Gaseous Phase and Electrochemical Hydrogen Storage Properties of $Ti_{50}Zr_1Ni_{44}X_5$ (X = Ni, Cr, Mn, Fe, Co, or Cu) for Nickel Metal Hydride Battery Applications

Jean Nei [1] and Kwo-Hsiung Young [1,2,*]

[1] BASF/Battery Materials-Ovonic, 2983 Waterview Drive, Rochester Hills, MI 48309, USA; jean.nei@basf.com
[2] Department of Chemical Engineering and Materials Science, Wayne State University, Detroit, MI 48202, USA
* Correspondence: kwo.young@basf.com; Tel.: +1-248-293-7000

Abstract: Structural, gaseous phase hydrogen storage, and electrochemical properties of a series of the $Ti_{50}Zr_1Ni_{44}X_5$ (X = Ni, Cr, Mn, Fe, Co, or Cu) metal hydride alloys were studied. X-ray diffraction (XRD) and scanning electron microscopy (SEM) revealed the multi-phase nature of all alloys, which were composed of a stoichiometric TiNi matrix, a hyperstoichiometric TiNi minor phase, and a Ti_2Ni secondary phase. Improvement in synergetic effects between the main TiNi and secondary Ti_2Ni phases, determined by the amount of distorted lattice region in TiNi near Ti_2Ni, was accomplished by the substitution of an element with a higher work function, which consequently causes a dramatic increase in gaseous phase hydrogen storage capacity compared to the $Ti_{50}Zr_1Ni_{49}$ base alloy. Capacity performance is further enhanced in the electrochemical environment, especially in the cases of the $Ti_{50}Zr_1Ni_{49}$ base alloy and $Ti_{50}Zr_1Ni_{44}Co_5$ alloy. Although the TiNi-based alloys in the current study show poorer high-rate performances compared to the commonly used AB_5, AB_2, and A_2B_7 alloys, they have adequate capacity performances and also excel in terms of cost and cycle stability. Among the alloys investigated, the $Ti_{50}Zr_1Ni_{44}Fe_5$ alloy demonstrated the best balance among capacity (394 mAh·g^{-1}), high-rate performance, activation, and cycle stability and is recommended for follow-up full-cell testing and as the base composition for future formula optimization. A review of previous research works regarding the TiNi metal hydride alloys is also included.

Keywords: hydrogen absorbing materials; metal hydride electrode; nickel/metal hydride (Ni/MH) battery; transition metal alloy; synergetic effects; electrochemistry; pressure-concentration-temperature (PCT) isotherm

1. Introduction

Nickel/metal hydride (Ni/MH) batteries have been used commercially for more than 25 years since their debut in 1989 by Ovonic, Matsushita, and Sanyo. Ni/MH batteries were once very popular for consumer applications, which have since largely shifted to Li-ion battery. Moreover, high-power Ni/MH battery technology is still the choice of today's hybrid electric vehicles. Presently, the same battery chemistry is entering into the market of stationary applications, which require a wide temperature range and a durable cycle stability [1,2]. This market is currently dominated by a less environmentally safe chemistry, lead-acid battery. However, comparison between General Motors EV1 electric vehicles powered by the lead-acid and Ni/MH battery packs reveals that using the Ni/MH battery technology not only nearly doubles the driving range with its higher energy density, but it also offers longer service life [3,4]. Those two proven advantages make Ni/MH battery technology a great contender for the stationary market. In fact, the only advantage lead-acid battery has compared

to Ni/MH battery is cheaper price. Therefore, there is a large driving force for cost-efficiency in the development of novel Ni/MH battery technology. One of the major components in Ni/MH battery is the negative electrode, which is an intermetallic compound that is capable of hydrogen storage, or in other words, a metal hydride (MH) alloy. Hydrogen storage intermetallic compounds have been extensively reviewed according to alloy type, application, and hydrogen absorption mechanism recently [5–12]. Among the many candidates of MH alloys [10], both the Ti-Ni and Mg-Ni systems have an advantage with regard to cost. The Mg-Ni-based MH alloys, being the cheapest, suffer from a severe capacity degradation with the current 30 wt% KOH electrolyte, leaving the Ti-Ni alloy system as the next choice for cost reduction. Raw material cost for 99.6% pure Ti sponge is approximately $8/kg, which is a very attractive alternative to the more expensive Zr or unstably priced rare earth elements used in today's Ni/MH battery.

The earliest Ni/MH batteries were demonstrated in the early 1970s and based on the Ti-Ni MH alloy system [13,14]. However, the first commercial Ni/MH battery products were fabricated with the misch metal-based AB_5 and transition metal-based disorder AB_2 MH alloys due to their improvements in cycle life. According to the Ti-Ni binary phase diagram [15], two intermetallic compounds can be used as hydrogen storage alloys: TiNi and Ti_2Ni. To achieve an optimal balance between storage capacity and high-rate dischargeability (HRD) for room-temperature battery operation, a stoichiometry of B/A close to two is ideal for the TiZrNi-based AB_2 MH alloys (Figure 1). With regard to a pure Ti-Ni system, however, eliminating Zr means that the B/A ratio must be reduced since the heat of hydride formation (ΔH_h) of Ti is higher than ΔH_h of Zr [16]. Therefore, TiNi is the better selection of the two available Ti-Ni intermetallic compounds. In addition, chemical modification can be adopted to further adjust the metal-hydrogen bond strength. The introduction of other elements can also increase the chance of secondary phase formation and consequently increase the electrochemical capacity through synergetic effects [17].

TiNi is a shape memory alloy. Upon cooling, TiNi is first solidified into a B2 cubic structure (austenite) and later to a B19' monoclinic structure (martensite). The shape at higher temperatures (austenite) is memorized and restored after thermal treatment to the deformed alloy with a martensite structure. Previous research efforts for electrochemical applications with the TiNi alloys are summarized in Table 1. While earlier works focused on the alloys produced by arc melting, induction melting, or other bulk ingot production methods, later works focused more on the powder produced by mechanical alloying. With the severe cycle stability problems observed in the MgNi-based MH alloys prepared by a combination of melt spinning and mechanical alloying [18], we choose induction melting as our first alloy preparation method for the current study. Furthermore, the substitution effects from various transition metals on the structural, gaseous phase, and electrochemical properties are investigated in this study.
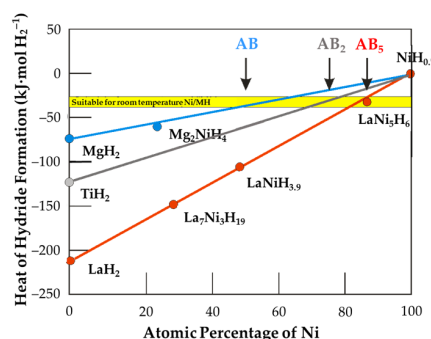

Figure 1. Plot of the heat of hydride formation for metal hydride vs. the corresponding Ni-content. Hydride formers, such as Mg, Ti, and La, have metal-hydrogen bonds that are too strong for room temperature nickel/metal hydride (Ni/MH) battery applications (a ΔH_h between -25 kJ·mol H_2^{-1} and -40 kJ·mol H_2^{-1} is desirable). Therefore, alloying hydride formers with Ni can adjust the bond strength and increase the electrochemical activity.

Table 1. Summaries of prior research on the TiNi-based MH alloys for electrochemical applications in chronological order. Preparation methods SN, AM, PM, IM, CO, MC, MA, ANN, MS, CHR, and MWCNT denote sintering, arc melting, melting in plasma furnace, induction melting, co-precipitation, microencapsulation, mechanical alloying, annealing, melt spinning, calcium hydride reduction, and multiwall carbon nanotube, respectively. TiNi phase structures B2, B19′, B19, and R are cubic, monoclinic, orthorhombic, and tetragonal, respectively. HRD: high-rate dischargeability.

Alloy Formula	Preparation Method	TiNi Phase Structure	Main Discoveries	Reference
$Ti_{53.6}Ni_{46.4}$	-	-	• The first TiNi-based metal hydride electrode	[19]
TiNi	SN	B2	• Capacity of 210 to 250 mAh·g^{-1} at C/10 rate • 67% of capacity is obtained at 1C rate at −30 °C	[13]
$TiNi + Ti_2Ni$	SN	B2	• Capacity of 300 to 320 mAh·g^{-1}	[13]
TiNi	SN	B2	• Capacity of 180 mAh·g^{-1} at 50 mA·g^{-1}	[14]
TiNi	AM	-	• Cyclic voltammetry study	[20]
$TiNi_x$ (x = 0.5–1.0)	SN vs. PM	-	• Higher capacity for SN alloy • Higher corrosion resistance for PM alloy • Increased cycle stability with increasing Ni-content	[21]
$Ti_{0.8}Zr_{0.2}Ni_x$ (x = 0.5–1.0)	SN vs. PM	-	• Increased capacity and cycle stability with Zr-substitution	[21]
TiNi	SN	-	• Increased surface reactivity with 1 M HF treatment	[22]
$Ti_{1-y}Zr_yNi_x$ (x = 0.50–1.45, y = 0–1.0)	SN	B2	• As the Zr-content (y) increases, maximized capacity occurs at higher Ni-content (x) • Capacity of 260 mAh·g^{-1} for $Ti_{0.9}Zr_{0.1}Ni_{1.0}$	[23]
$Ti_{0.5}Zr_{0.5}Ni_{0.95-x}Cu_{0.05+x}$ (x = 0–0.05)	SN	B2	• Increased cycle stability with increasing Cu-content	[23]
$TiNi_{0.9}B_{0.1}$	SN	-	• B does not prevent segregation of Ti during cycling	[24]
$Ti_{0.7}Zr_{0.2}V_{0.1}Ni$	IM	B2	• Capacity of 350 mAh·g^{-1} at 30 mA·g^{-1}	[25]
TiNi	CO + SN	-	• Oxygen consumption reaction study	[26]
TiNi	-	B2 vs. B19′	• Capacities of 168 mAh·g^{-1} and 176 mAh·g^{-1} at 50 mA·g^{-1} for B19′ and B2 TiNi, respectively	[27]
TiNi	AM	-	• Cycling model determined by both thermal dynamic and kinetic degradations	[28]
TiNi + 5% M (M = Ni, Cu)	SN + MC	-	• Capacity of 150 mAh·g^{-1} at 30 mA·g^{-1} for TiNi • Increased capacity with Ni- (180 mAh·g^{-1}) or Cu-addition (169 mAh·g^{-1}) • Increased HRD with Cu	[29]
$TiNi_{0.5}Fe_{0.5}$	AM vs. MA	-	• Capacities of 65 and 190 mAh·g^{-1} at 20 mA·g^{-1} for AM and MA alloys, respectively	[30]
$TiNi_{0.6}Fe_{0.4}$	AM vs. AM + MA vs. MA	B2	• Capacities of 108, 138, 161 mAh·g^{-1} at 30 mA·g^{-1} for AM, AM + MA, and MA alloys, respectively • MA alloy demonstrates the best activation and the worst cycle stability	[31]

Table 1. *Cont.*

Alloy Formula	Preparation Method	TiNi Phase Structure	Main Discoveries	Reference
$Ti_{50}Ni_{41}Nb_9$	AM	B2	• Increased capacity and cycle stability with Nb-substitution	[32]
TiNi	AM	-	• Study on parameters affecting discharge capacity and cycle life	[33]
TiNi	AM	-	• Study on parameters affecting discharge kinetics	[34]
$Ti_{0.7}Zr_{0.2}V_{0.1}Ni$	AM + ANN	B2	• Capacity of 180 mAh·g^{-1} at 50 mA·g^{-1} for TiNi • Increased capacity due to secondary Laves phase formation but harder activation for $Ti_{0.7}Zr_{0.2}V_{0.1}Ni$ (205 mAh·g^{-1})	[35]
Mg_2Ni + TiNi	MA	B2	• Increased cycle stability compared to Mg_2Ni	[36]
$Ti_{50-x}Zr_xNi_{50}$ (x = 0–24)	IM vs. MS	B19′ for IM alloy vs. B2 for MS alloy	• Capacity of 335 mAh·g^{-1} at C/10 rate for B19′ $Ti_{32}Zr_{18}Ni_{50}$	[37]
$TiNi_xFe_{1-x}$ (x = 0–1.0)	MA + ANN	B2	• Capacity of 67 mAh·g^{-1} at 40 mA·g^{-1} for TiNi • Increased capacity but decreased cycle stability with Fe-substitution (155 mAh·g^{-1} for $TiNi_{0.75}Fe_{0.25}$)	[38]
(Ti + Ni)	MA under H_2	-	• Capacity of 150 mAh·g^{-1} at 50 mA·g^{-1} for 45-h-MA alloy with good cycle stability	[39]
$Ti_{0.5}Ni_{0.25}Al_{0.25}$	IM	B2	• Two discharge plateaus observed due to alloy's multi-phase nature	[40]
Ti(Ni,Fe,Mo,Cr,Co)	MA + ANN	B2	• Increased cycle stability for $TiNi_{0.6}Fe_{0.1}Mo_{0.1}Cr_{0.1}Co_{0.1}$ (135 mAh·g^{-1} at 40 mA·g^{-1}) compared to $TiNi_{0.75}Fe_{0.25}$	[41]
Ti(Ni,Fe,Mo,Cr,Co)	AM + ANN vs. MA + ANN	B2	• Increased capacity with MA + ANN • Increased cycle stability for $TiNi_{0.6}Fe_{0.1}Mo_{0.1}Cr_{0.1}Co_{0.1}$ (150 mAh·g^{-1} at 40 mA·g^{-1}) compared to $TiNi_{0.75}Fe_{0.25}$	[42]
Mg_2Ni + TiNi	MA vs. MA + ANN	B2	• Increased cycle stability with ANN	[43]
(Ti,Zr,V,Cr,Mn)Ni	AM	B2	• Increased capacity and HRD due to secondary Laves phase formation but harder activation with Mn- and/or Cr-substitutions (232 mAh·g^{-1} at 50 mA·g^{-1} for $Ti_{0.6}Zr_{0.2}V_{0.1}Mn_{0.1}Ni$)	[44]
$TiNi_{0.75}Fe_{0.25}$	MA + ANN	B2	• 1.5 fold increased capacity with Fe-substitution in sealed battery	[45]
Ti(Ni,Fe,Zr)	MA + ANN	B2	• Capacity of 79 mAh·g^{-1} at 40 mA·g^{-1} for TiNi • Increased capacity with Zr-substitution (135 mAh·g^{-1} for $TiNi_{0.875}Zr_{0.125}$) • Increased capacity but decreased cycle stability with Fe-substitution (158 mAh·g^{-1} for $TiNi_{0.75}Zr_{0.125}Fe_{0.125}$)	[46]
TiNi	CHR vs. CHR + ANN	B2 + B19′ for CHR alloy vs. B2 for CHR + ANN alloy	• Capacity of 125 mAh·g^{-1} at 50 mA·g^{-1} for B2 TiNi • Increased capacity due to dual-phase nature for B2 + B19′ TiNi (160 mAh·g^{-1})	[47]

Table 1. *Cont.*

Alloy Formula	Preparation Method	TiNi Phase Structure	Main Discoveries	Reference
$TiNi_{1-x}M_x$ (M = Mg, Mn, Zr, x = 0–0.25)	MA + ANN	B2	• Increased capacity but slightly decreased cycle stability with Mg- (152 mAh·g^{-1} at 40 mA·g^{-1}) or Mn-substitution (153 mAh·g^{-1}) compared to Zr-substitution (135 mAh·g^{-1}) • Decreased cycle stability with higher Mn-substitution	[48]
Ti (Ni, Fe, Zr, Mo, Cr, Co, Al)	MA + ANN	B2	• Increased capacity with all substitutions in the order of Co (113 mAh·g^{-1} at 40 mA·g^{-1}) < Mo < Al < Cr < Fe (155 mAh·g^{-1}) • Decreased cycle stability with all substitutions in the order of Co < Cr < Fe ≈ Al < Mo (worst) • 1.5 fold increased capacity with Fe-substitution or Fe-, Co-, and Zr-substitutions in sealed battery	[49]
$TiNi_{1-x}M_x$ (M = Co, Fe, Sn, x = 0–0.2)	MA vs. MA + ANN	-	• Capacities of 52 and 67 mAh·g^{-1} at 40 mA·g^{-1} for MA and MA + ANN TiNi, respectively, with good cycle stability • Increased capacity with ANN • Harder activation with ANN • Increased capacity with Co- (83 mAh·g^{-1} with ANN) or Fe-substitution (79 mAh·g^{-1} with ANN)	[50]
Ti (Ni, Fe, Zr, Mo, Cr, Co)	MA	B2	• Increased capacity and cycle stability with Fe-substitution in sealed battery • Increased cycle stability with Zr-substitution in sealed battery	[51]
$Ti_{0.8}M_{0.2}Ni$ (M = Zr, V)	MA vs. MA + ANN	B2	• Decreased capacity with Zr- or V-substitution	[52]
$TiNi_{0.8}M_{0.2}$ (M = Cu, Mn)	MA vs. MA + ANN	-	• Decreased capacity with Cu-substitution • Increased capacity with Mn-substitution (75 mAh·g^{-1} at 40 mA·g^{-1} with ANN)	[52]
$TiNi_{1-x}Mn_x$ (x = 0.2–1.0)	MA vs. MA + ANN	-	• Decreased capacity with higher Mn-substitution	[52]
$Ti_{1.02-x}Zr_xNi_{0.98}$ (x = 0–0.48)	IM + ANN	B19′	• Capacity of 150 mAh·g^{-1} at C/10 rate for TiNi • Increased capacity with Zr-substitution due to the difference in martensitic transformation (350–370 mAh·g^{-1} for $Ti_{0.78}Zr_{0.24}Ni_{0.98}$)	[53]
$TiNi_{0.8}B_{0.2}$, $Ti_{0.8}B_{0.2}Ni$,	MA vs. MA + ANN	B2	• Decreased capacity with B-substitution, and further decrease with ANN	[54]
$Ti_{1.02-x}Zr_xNi_{0.98}$ (x = 0–0.48)	IM + ANN	B19′	• Harder activation with higher Zr-substitution • Decreased cycle stability with Zr-substitution	[55]
TiNi	SN (750–950 °C)	B2	• Increased capacity and HRD with higher SN temperature (179–211 mAh·g^{-1} at 60 mA·g^{-1})	[56]

Table 1. *Cont.*

Alloy Formula	Preparation Method	TiNi Phase Structure	Main Discoveries	Reference
TiNi	SN	B2	• Capacity of 205 mAh·g^{-1} at 60 mA·g^{-1}	[57]
TiNi	MA (20–60 h)	-	• Capacity of 102 mAh·g^{-1} at 60 mA·g^{-1} with bad cycle stability	[58]
TiNi	MA vs. MA + ANN	B2	• Higher capacity for crystalline TiNi (150 mAh·g^{-1} with ANN).	[59]
Mg$_2$Ni + TiNi	MA	B2	• Decreased capacity compared to Mg$_2$Ni.	[60]
Ti$_{1.04}$Ni$_{0.96-x}$Pd$_x$ (x = 0–0.5)	IM + ANN	As x increases, B2 + B19′ → B2 + B19′ + R → B2 + B19	• Decreased capacity with Pd-substitution (148 and 84 mAh·g^{-1} at C/5 rate for x = 0.1 and 0.4, respectively)	[61]
Sn-doped TiNi	Thin film sputtering	-	• TiNi-based anode for Li-ion battery	[62]
TiNi	MA	-	• TiNi-based anode for Li-ion battery	[63]
TiNi-5 wt% Pd + 5 wt% MWCNT	MA + ANN + MA with MWCNT	B2	• Capacity of 171 mAh·g^{-1} at 40 mA·g^{-1} for TiNi • Increased capacity and cycle stability with Pd- (186 mAh·g^{-1}), MWCNT- (183 mAh·g^{-1}), or Pd + MWCNT-addition (266 mAh·g^{-1})	[64]
(TiNi)$_{1-x}$Mg$_x$ (x = 0–0.3)	MA (10 to 40 h)	B2	• Increased and then decreased capacity and increased cycle stability with increasing MA time for TiNi (~132 mAh·g^{-1} at 40 mA·g^{-1}) • Decreased capacity with Mg-incorporation	[65]
Ti$_{1.01}$Ni$_{0.99-x}$Cu$_x$ (x = 0–0.5)	IM + ANN	As x increases, B19′ → B19	• Increased and then decreased capacity with increasing Cu-content (300 mAh·g^{-1} at C/10 rate for Ti$_{1.01}$Ni$_{0.79}$Cu$_{0.2}$) • Increased HRD with Cu-substitution	[66]
MgTiNi$_2$	MA	-	• Capacity of 93 mAh·g^{-1} at 40 mA·g^{-1}	[67]
Ti$_{1-x}$Zr$_x$Ni (x = 0–0.5)	MA + ANN	B2	• Increased and then decreased capacity and increased cycle stability with increasing Zr-content (192 mAh·g^{-1} at 40 mA·g^{-1} for Ti$_{0.75}$Zr$_{0.25}$Ni)	[68]
Ti$_{0.75}$Zr$_{0.25}$Ni-5 wt% Pd vs. Ti$_{0.75}$Zr$_{0.25}$Ni + 5 wt% Pd	MA + ANN vs. MA + ANN + MA with Pd	B2	• Increased capacity with Pd-addition • Early addition of Pd (223 mAh·g^{-1}) has higher capacity than later addition (208 mAh·g^{-1})	[68]

2. Experimental Setup

Each alloy sample was prepared in a 2-kg induction furnace with an $MgAl_2O_4$ crucible, an alumina tundish, and a pancake-shaped steel mold under an argon atmosphere. Chemical composition for the ingot was analyzed using a Varian Liberty 100 inductively coupled plasma optical emission spectrometer (ICP-OES, Agilent Technologies, Santa Clara, CA, USA). A Philips X'Pert Pro X-ray diffractometer (XRD, Amsterdam, The Netherlands) was used to study the microstructure, and a JEOL-JSM6320F scanning electron microscope (SEM, Tokyo, Japan) with energy dispersive spectroscopy (EDS) capability was used to study the phase distribution and composition. Gaseous phase hydrogen storage characteristics for each sample were measured using a Suzuki-Shokan multi-channel pressure-concentration-temperature (PCT, Tokyo, Japan) system. For the PCT analysis, each sample (a single piece of ingot with newly cleaved surfaces and a weight of about 4–5 g) was first activated by several thermal cycles between 300 °C and room temperature under 2.5 MPa H_2 pressure. PCT isotherms at 90 °C and 120 °C were then measured. Details of the electrode and cell preparations, as well as the electrochemical measurement methods, have been previously reported [18,69]. Magnetic susceptibility was measured using a Digital Measurement Systems Model 880 vibrating sample magnetometer (MicroSense, Lowell, MA, USA).

3. Results

3.1. Alloy Preparation

Six alloys with the design compositions $Ti_{50}Zr_1Ni_{44}X_5$ (X = Ni, Cr, Mn, Fe, Co, or Cu) were prepared by induction melting. A slightly hypostoichiometric TiNi formulation with a small addition of Zr (has a higher metal-hydrogen bond strength compared to Ti) in the A-site was adopted to increase the degree of disorder (DOD) and consequently improve the electrochemical properties. Zr is also an oxygen scavenger, forming oxide slag in the melt that can be separated by the tundish [70]. Furthermore, adding Zr can possibly reduce capacity degradation by suppressing passivation caused by the thick TiO_2 surface oxide layer [71]. Compositions of the six alloys, verified by ICP and shown in Table 2, are very close to their design values.

Table 2. Design compositions (in **bold**) and inductively coupled plasma (ICP) results (in at %). B/A is the atomic ratio of B-atom (elements other than Ti and Zr) to A-atom (Ti and Zr).

Alloy TN-X	Source	Ti	Zr	Ni	X	B/A
TN-Ni	**Design**	**50.0**	**1.0**	**49.0**	**-**	**0.96**
	ICP	50.0	0.6	49.4	0.0	0.98
TN-Cr	**Design**	**50.0**	**1.0**	**44.0**	**5.0**	**0.96**
	ICP	49.7	1.1	44.4	4.7	0.97
TN-Mn	**Design**	**50.0**	**1.0**	**44.0**	**5.0**	**0.96**
	ICP	49.2	1.0	44.9	4.9	0.99
TN-Fe	**Design**	**50.0**	**1.0**	**44.0**	**5.0**	**0.96**
	ICP	49.9	1.0	44.3	4.8	0.96
TN-Co	**Design**	**50.0**	**1.0**	**44.0**	**5.0**	**0.96**
	ICP	49.8	0.9	44.5	4.8	0.97
TN-Cu	**Design**	**50.0**	**1.0**	**44.0**	**5.0**	**0.96**
	ICP	49.5	1.3	44.5	4.7	0.97

3.2. X-Ray Diffraction Analysis

XRD patterns of the six alloys are shown in Figure 2. Two sets of diffraction peaks, the main TiNi phase with a B2 cubic structure (belonging to the space group $Pm\bar{3}m$) and the secondary Ti_2Ni phase with an $E9_3$ face-centered cubic structure (belonging to the space group $Fd\bar{3}m$), are observed in all alloys. Crystal structures of TiNi and Ti_2Ni generated by the XCrySDen software [72] are shown in Figure 3.
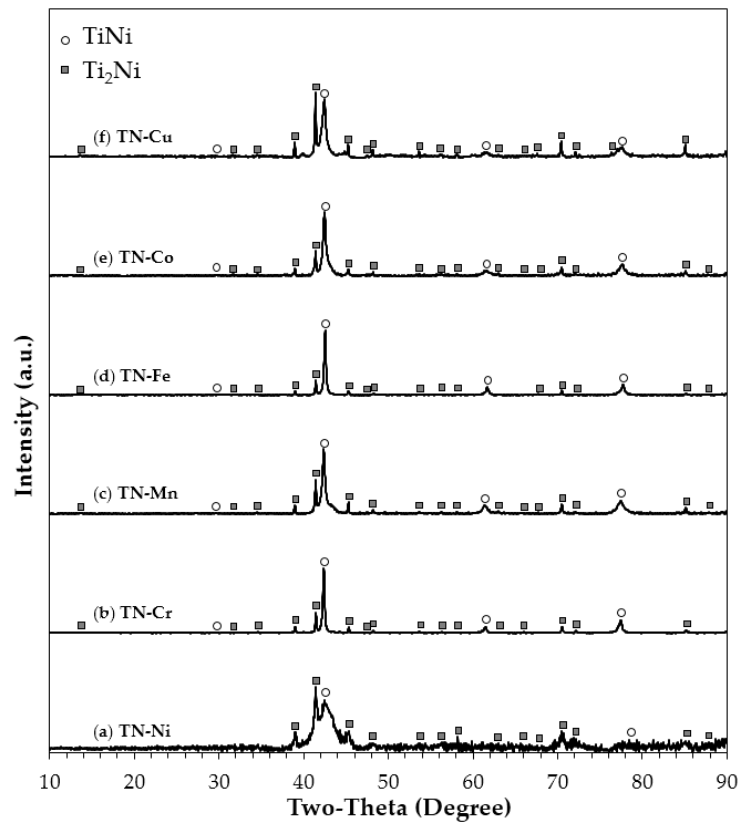
Figure 2. X-ray diffraction (XRD) patterns using Cu-Kα as the radiation source for alloys: (**a**) TN-Ni; (**b**) TN-Cr; (**c**) TN-Mn; (**d**) TN-Fe; (**e**) TN-Co; and (**f**) TN-Cu. Besides the main TiNi phase with a cubic B2 structure, a secondary Ti$_2$Ni phase with a cubic structure and a larger lattice constant can be also identified.
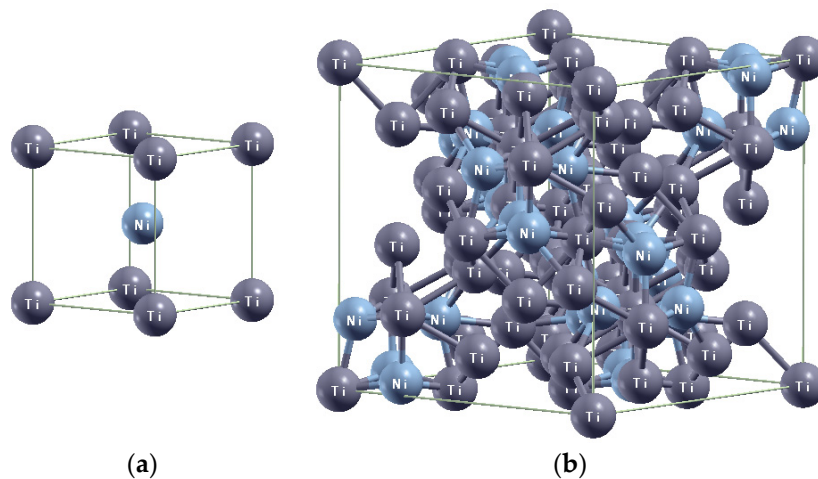

Figure 3. Crystal structures of (**a**) TiNi with a B2 cubic structure and (**b**) Ti$_2$Ni with an E9$_3$ face-centered cubic structure generated using the XCrySDen software [72].

Full XRD pattern fitting was performed using the Rietveld refinement and Jade 9 Software to obtain the lattice parameters, crystallite sizes, and phase abundances, and the results are listed in Table 3. Lattice constant *a* of the TiNi phase in alloy TN-Ni is smaller than that found in the stoichiometric TiNi alloy [73]. Although the overall alloy formulation is hypostoichiometric, formation of the Ti$_2$Ni phase increases the B/A ratio in the TiNi phase, which contributes to the reduction in its

lattice constant from that of the stoichiometric TiNi phase due to either Ni into Ti-anti-site or Ti-vacancy defects. Lattice constants *a*'s of TiNi in all substituted alloys are larger than that in the base alloy TN-Ni. Since all substituting elements are larger than Ni but much smaller than Ti, they occupy the Ni-site and increase the lattice constant. In Figure 4a, TiNi lattice constant *a* is correlated with the atomic radius of substituting element in the Laves phase [74] (a value used to simulate the size of substituting element in the TiNi phase), and a linear dependency can be observed. However, such correlation is not seen in the plot of Ti_2Ni lattice constant *a* versus the atomic radius of substituting element in the Laves phase (Figure 4b), which is due to the change in B/A ratio of the Ti_2Ni phase from 0.51 to 0.70 as revealed by SEM/EDS (see Section 3.3). All alloys show similar TiNi/Ti_2Ni abundance ratios except for alloys TN-Ni and TN-Cu, where the Ti_2Ni phase abundance is higher than those in other alloys. Moreover, crystallite sizes of TiNi and Ti_2Ni were estimated by the Scherrer equation [75] using the full widths at half maximum of the TiNi (110) peak and Ti_2Ni (511) peak in the XRD patterns, and the results are listed in Table 3. Both the crystallite sizes of the TiNi and Ti_2Ni phases in the base alloy TN-Ni are much smaller than those in the substituted alloys. Partial replacement of Ni with other elements may increase the peritectic temperature [76], leaving more time for the crystallites to grow.
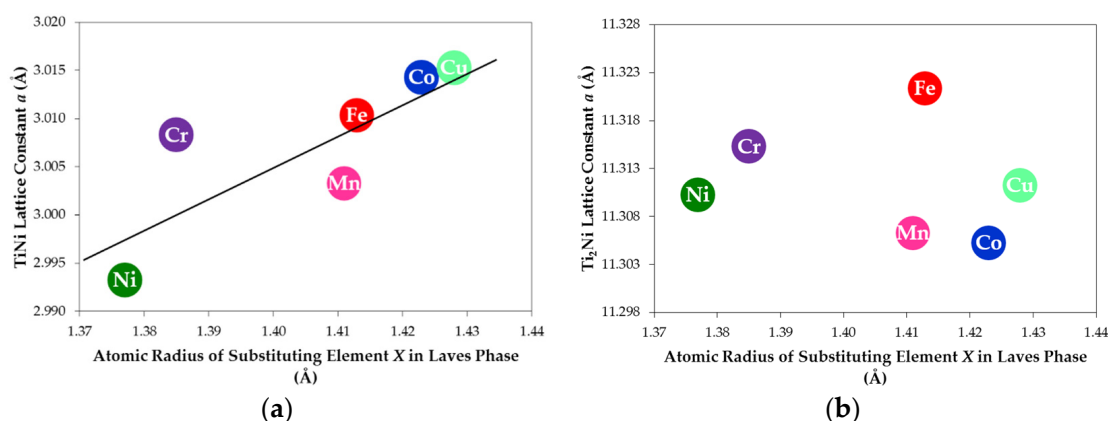

Figure 4. Plots of the (**a**) TiNi lattice constant *a*; and (**b**) Ti_2Ni lattice constant *a* vs. the atomic radius of substituting element *X* in the Laves phase (data from [74]). A linear correlation is observed for the TiNi lattice constant but not for the Ti_2Ni lattice constant.

Table 3. Summary of XRD analysis (lattice constants, phase abundances, and crystallite sizes).

Alloy TN-*X*	*a* of TiNi (Å)	*a* of Ti_2Ni (Å)	TiNi Abundance (wt%)	Ti_2Ni Abundance (wt%)	TiNi Crystallite Size (Å)	Ti_2Ni Crystallite Size (Å)
TN-Ni	2.993	11.310	68.7	31.3	139	448
TN-Cr	3.014	11.305	75.5	24.5	368	804
TN-Mn	3.015	11.311	78.4	21.6	251	>1000
TN-Fe	3.003	11.306	80.7	19.3	346	812
TN-Co	3.008	11.315	80.6	19.4	212	655
TN-Cu	3.010	11.321	71.6	28.4	206	727

3.3. Scanning Electron Microscopy/Energy Dispersive Spectroscopy Study

Microstructures of the six alloys were studied using SEM, and the resulting 100× and 1000× back-scattering electron images (BEI) are shown in Figures 5 and 6, respectively. BEI images demonstrate the changes in both surface morphology and contrast due to the difference in average atomic weight. EDS was used to study the chemical compositions of several areas with different contrasts identified numerically in the micrographs (Figure 6), and the results are summarized in Table 4. Basically, three different contrasts are observed and assigned to a TiNi-2 (brightest), a TiNi-1 (matrix), and a Ti_2Ni (darkest) phases. Although the grain size of the Ti_2Ni phase varies and increases

in the order of TN-Fe < TN-Ni ≈ TN-Cr < TN-Cu < TN-Mn ≈ TN-Co (Figures 5 and 6), the six alloys show similar phase distributions:

- Matrix (TiNi-1): stoichiometric or slightly hyperstoichiometric TiNi with the Zr- and *X*-contents close to design.
- Minor phase (TiNi-2): this phase appears as bright spots in the micrographs and is distributed within the matrix. It is generally hyperstoichiometric, high-Zr, and high-*X* TiNi except for:

    ○ Hypostoichiometric, high-Zr, and close to the design-X TiNi in alloy TN-Fe and
    ○ Hyperstoichiometric, high-Zr, and low-X TiNi in alloy TN-Co.

- Secondary phase (Ti_2Ni): this phase has the darkest contrast in the micrographs and appears next to the main TiNi-1 phase. It is stoichiometric or hyperstoichiometric, low-Zr Ti_2Ni.
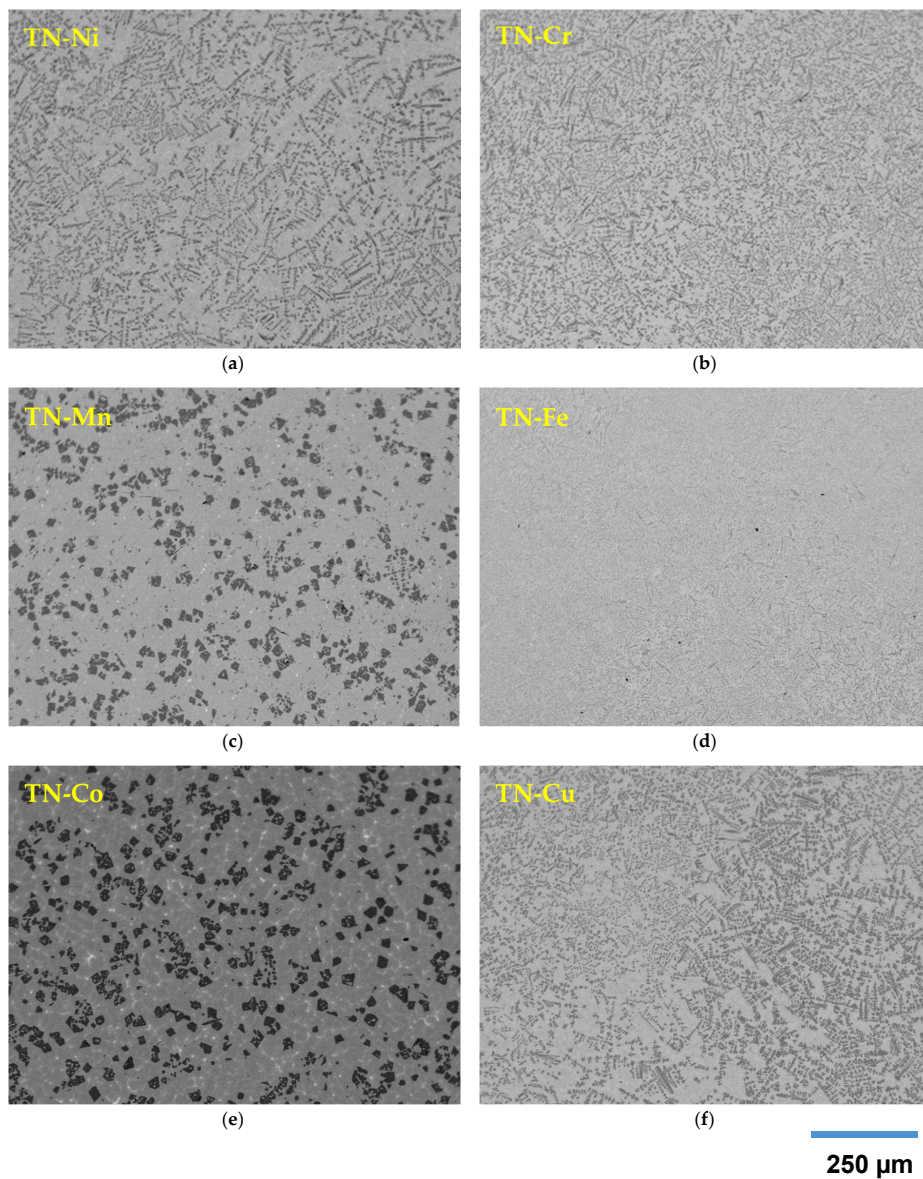

Figure 5. Scanning electron microscopy (SEM) × back-scattering electron images (BEI) micrographs from alloys: (**a**) TN-Ni; (**b**) TN-Cr; (**c**) TN-Mn; (**d**) TN-Fe; (**e**) TN-Co; and (**f**) TN-Cu at 100× magnification.

Figure 6. SEM BEI micrographs from alloys: (**a**) TN-Ni; (**b**) TN-Cr; (**c**) TN-Mn; (**d**) TN-Fe; (**e**) TN-Co; and (**f**) TN-Cu at 1000× magnification.

According to the Ti-Ni binary phase diagram [15], as the melt of $Ti_{51}Ni_{49}$ cools to 1310 °C, a hyperstoichiometric TiNi phase, or TiNi-2 in the current study, initially forms due to the TiNi system's preference for hyperstoichiometry (as seen from the wide solubility range of the TiNi phase towards hyperstoichiometric TiNi in the phase diagram). Once the system reaches the temperature of 984 °C, the hyperstoichiometric TiNi-2 phase and rest of the melt goes through a peritectic reaction, which consumes most of the TiNi-2 phase and produces the final stoichiometric TiNi (TiNi-1) and Ti_2Ni phases. Ti_2Ni precipitated within the main TiNi matrix was found to deteriorate the alloy's mechanical properties for engineering applications due to its brittleness [77], but Ti_2Ni can be advantageous for initial pulverization for the use in electrochemical applications. Moreover, the presence of T_2Ni as the secondary phase in the TiNi alloy system was shown to be essential for electrochemical property improvement [14].

Table 4. Summary of EDS results. All compositions are in at%. Compositions of the **main TiNi-1**, minor TiNi-2, and *secondary Ti₂Ni* phases are in **bold**, underline, and *italic*, respectively.

Alloy TN-*X*	Area	Ti	Zr	Ni	*X*	B/A	Phase(s)
TN-Ni	1	36.3	8.4	55.3	0.0	1.24	TiNi-2
	2	40.9	4.7	54.3	0.0	1.19	TiNi-2
	3	44.2	2.3	53.5	0.0	1.15	TiNi-2
	4	42.4	3.4	54.2	0.0	1.18	TiNi-2
	5	**46.9**	**0.6**	**52.5**	**0.0**	**1.11**	**TiNi-1**
	6	**47.5**	**0.5**	**52.0**	**0.0**	**1.08**	**TiNi-1**
	7	*64.2*	*0.5*	*35.3*	*0.0*	*0.55*	*Ti₂Ni*
	8	*63.6*	*0.4*	*36.0*	*0.0*	*0.56*	*Ti₂Ni*
TN-Cr	1	41.0	4.6	44.4	10.0	1.19	TiNi-2
	2	42.0	2.7	43.9	11.3	1.24	TiNi-2
	3	**47.5**	**0.9**	**47.6**	**4.0**	**1.07**	**TiNi-1**
	4	**46.3**	**1.4**	**46.9**	**5.4**	**1.10**	**TiNi-1**
	5	*62.2*	*0.8*	*33.3*	*3.7*	*0.59*	*Ti₂Ni*
TN-Mn	1	33.8	12.0	32.5	21.7	1.18	TiNi-2
	2	44.1	2.7	43.0	10.1	1.13	TiNi-2
	3	43.7	3.1	42.5	10.6	1.13	TiNi-2
	4	**46.6**	**1.0**	**46.2**	**6.1**	**1.10**	**TiNi-1**
	5	**47.0**	**0.8**	**46.7**	**5.5**	**1.09**	**TiNi-1**
	6	**49.0**	**0.6**	**45.3**	**5.0**	**1.01**	**TiNi-1**
	7	**46.5**	**1.0**	**47.0**	**5.5**	**1.11**	**TiNi-1**
	8	*65.3*	*0.6*	*32.4*	*1.7*	*0.52*	*Ti₂Ni*
	9	*65.0*	*0.6*	*32.5*	*1.9*	*0.52*	*Ti₂Ni*
TN-Fe	1	46.4	7.0	42.1	4.5	0.87	TiNi-2
	2	46.1	6.2	42.9	4.8	0.91	TiNi-2
	3	**47.2**	**1.3**	**46.3**	**5.2**	**1.06**	**TiNi-1**
	4	**46.8**	**2.2**	**45.9**	**5.2**	**1.04**	**TiNi-1**
	5	52.3	1.1	42.0	4.6	0.87	TiNi + Ti₂Ni
	6	52.4	1.2	41.6	4.8	0.87	TiNi + Ti₂Ni
	7	*62.8*	*0.9*	*32.6*	*3.7*	*0.57*	*Ti₂Ni*
	8	*57.8*	*1.0*	*37.1*	*4.1*	*0.70*	*Ti₂Ni*
TN-Co	1	29.4	13.7	55.6	1.3	1.32	TiNi-2
	2	29.4	13.3	55.8	1.4	1.34	TiNi-2
	3	37.2	26.6	33.1	3.2	0.57	(TiZr)₂Ni
	4	41.0	15.1	39.7	4.1	0.78	(TiZr)₂Ni
	5	40.6	5.0	51.7	2.7	1.19	TiNi-2
	6	43.9	2.8	49.7	3.5	1.14	TiNi-2
	7	**47.6**	**0.5**	**45.1**	**6.7**	**1.08**	**TiNi-1**
	8	**47.9**	**0.6**	**44.9**	**6.6**	**1.06**	**TiNi-1**
	9	*65.5*	*0.7*	*29.9*	*3.9*	*0.51*	*Ti₂Ni*
	10	*65.4*	*0.6*	*30.3*	*3.7*	*0.51*	*Ti₂Ni*
TN-Cu	1	29.1	10.7	41.0	19.1	1.51	TiNi-2
	2	34.7	9.1	40.1	16.0	1.28	TiNi-2
	3	34.0	30.5	31.0	4.5	0.55	(TiZr)₂Ni
	4	42.1	14.2	39.4	4.4	0.78	(TiZr)₂Ni
	5	43.7	2.9	46.5	6.8	1.14	TiNi
	6	44.5	2.4	47.1	6.0	1.13	TiNi
	7	**47.2**	**1.0**	**47.3**	**4.4**	**1.07**	**TiNi-1**
	8	**46.8**	**1.0**	**47.6**	**4.6**	**1.09**	**TiNi-1**
	9	*63.5*	*0.8*	*34.0*	*1.7*	*0.55*	*Ti₂Ni*
	10	*65.6*	*0.8*	*32.4*	*1.2*	*0.51*	*Ti₂Ni*

Unlike the relatively constant B/A ratio in the main TiNi-1 phase among alloys, that of the secondary Ti₂Ni phase ranges significantly, resulting in the inconsistency observed between the size of

substituting element and Ti$_2$Ni lattice constant. Solubility of Zr in the Ti$_2$Ni phase is less than those in the TiNi-1 and TiNi-2 phases. Such observations can be explained by the pseudo-binary phase diagrams for the TiNi-ZrNi and Ti$_2$Ni-Zr$_2$Ni systems [78], where the TiNi phase shows a very high solubility for Zr (up to approximately 30%) while Zr is nearly insoluble in the Ti$_2$N phase.

3.4. Pressure-Concentration-Temperature Measurement

Gaseous phase hydrogen storage properties of the six alloys were studied by PCT. Due to the slow reaction kinetics, PCT isotherm at 30 °C or 60 °C cannot be measured (absorption weight is approximately 0% at all applied H$_2$ pressures). Therefore, the absorption and desorption isotherms were measured at 90 °C and 120 °C and are shown in Figure 7. Information obtained from the PCT study is summarized in Table 5. At either temperature, both the maximum and reversible capacities following the trend of TN-Ni $\approx$ TN-Co < TN-Cu < TN-Mn < TN-Cr < TN-Fe, which demonstrates a very weak correlation to the main TiNi phase lattice constant as seen in Figure 8a. 90 °C gaseous phase maximum capacity is also plotted against ΔH_h of substituting element (Figure 8b), a value that is often taken into consideration during alloy design to achieve balance between the amounts of A-site hydride formers ($\Delta H_h < 0$) and B-site modifiers ($\Delta H_h > 0$). In the current study, the modification is performed on the B-site, and the expected trend is increasing capacity with decreasing ΔH_h of substituting element; however, no clear correlation is observed. ΔH_h of the AB$_n$ alloy can be calculated with the equation [79]:

$$\Delta H_h\left(AB_nH_{2m}\right) = \Delta H_h\left(AH_m\right) + \Delta H_h\left(B_nH_m\right) - \Delta H\left(AB_n\right) \tag{1}$$

where ΔH is the heat of alloy formation. The difference in trends for ΔH_h of substituting element and gaseous phase capacity is possibly caused by the heat of alloy formation. Finally, 90 °C gaseous phase maximum capacity is plotted against the work function (*W*, the difference between the electron potentials in vacuum (E_{VAC}) and the Fermi level (E_F)) of substituting element in Figure 8c, which illustrates a linear relationship. *W*'s of various phases in a multi-phase MH system have been used to explain the synergetic effects observed in the gaseous phase hydrogen interaction [17]. In the current study, the secondary Ti$_2$Ni phase with a lower ΔH_h and a higher *W* is hydrogenated first, which expands the lattice in the TiNi phase near the Ti$_2$Ni phase (pink region in Figure 9) due to the stress transmitted through the "coherent interface" and eases the hydrogenation of the main TiNi phase [80]. When a substituting element with a smaller *W* compared to Ni is added into the system, *W* of the main TiNi phase is reduced while *W* of the Ti$_2$Ni phase remains the same (as seen from Table 4, solubility of substituting element in Ti$_2$Ni is lower than that in TiNi), leading to an increase in difference between *W*'s of the two phases (Figure 9). This larger difference in *W*'s causes an increase in volume of initial hydrogenation of the secondary Ti$_2$Ni phase and therefore enlarges the volume of the expanded lattice region, resulting in a higher gaseous phase capacity. Moreover, alloy TN-Mn seems to fall off the linear trend slightly in Figure 8. Although Fe and Cr have higher *W*'s than Mn, their higher densities of interface between the main TiNi and secondary Ti$_2$Ni (Figures 5 and 6) contributes to the amount of distorted lattice zone and facilitates alloy hydrogenation.

Table 5. Summary of gaseous phase properties.

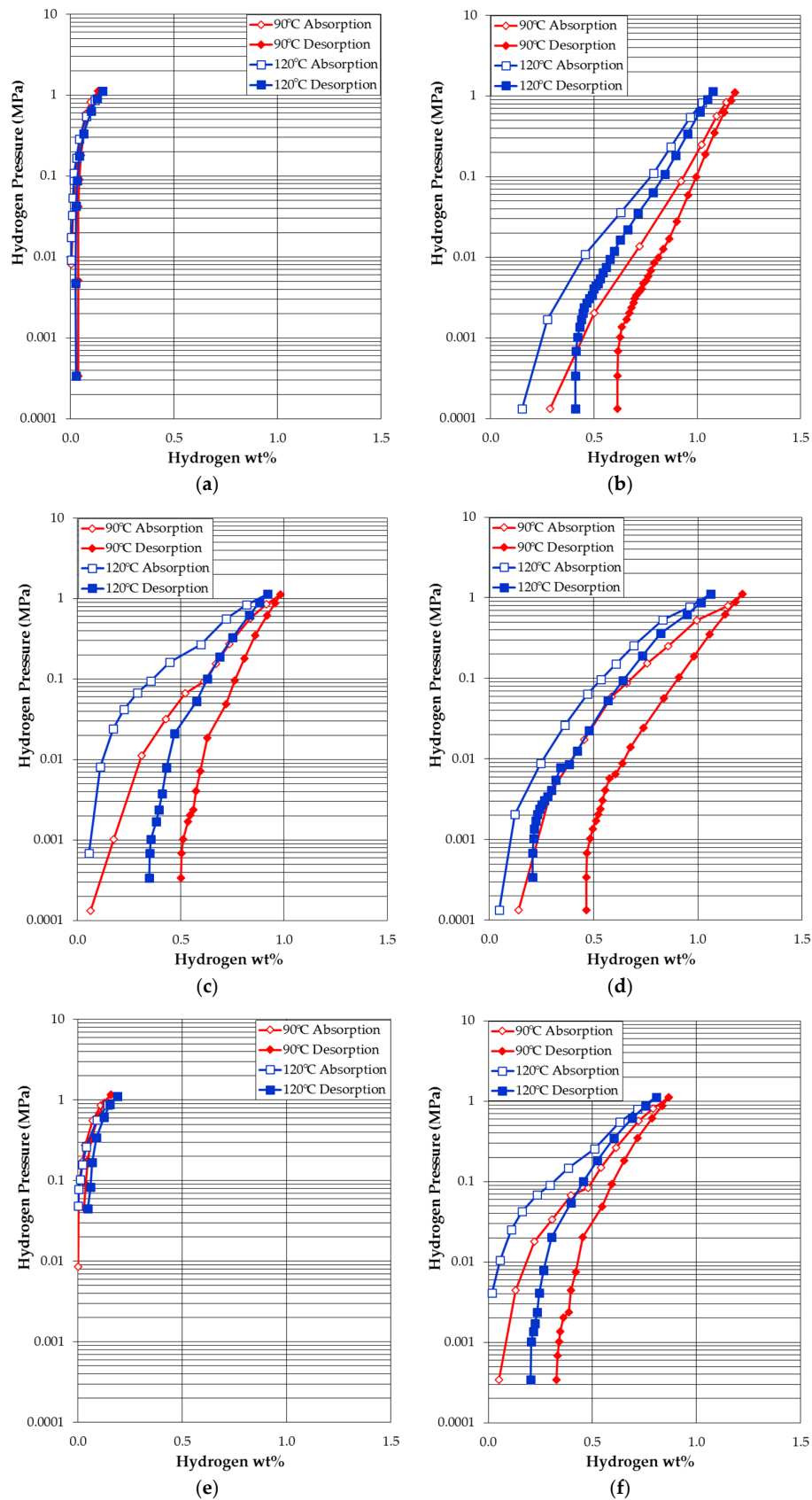| Alloy TN-*X*	Maximum Capacity at 90 °C (wt%)	Reversible Capacity at 90 °C (wt%)	Maximum Capacity at 120 °C (wt%)	Reversible Capacity at 120 °C (wt%)
TN-Ni	0.13	0.09	0.15	0.13
TN-Cr	1.18	0.57	1.08	0.67
TN-Mn	0.98	0.48	0.92	0.57
TN-Fe	1.21	0.75	1.06	0.85
TN-Co	0.16	0.13	0.19	0.14
TN-Cu	0.87	0.54	0.81	0.60

Figure 7. The 90 and 120 °C pressure-concentration-temperature (PCT) isotherms of alloys: (**a**) TN-Ni; (**b**) TN-Cr; (**c**) TN-Mn; (**d**) TN-Fe; (**e**) TN-Co; and (**f**) TN-Cu. Open and solid symbols are for absorption and desorption curves, respectively.
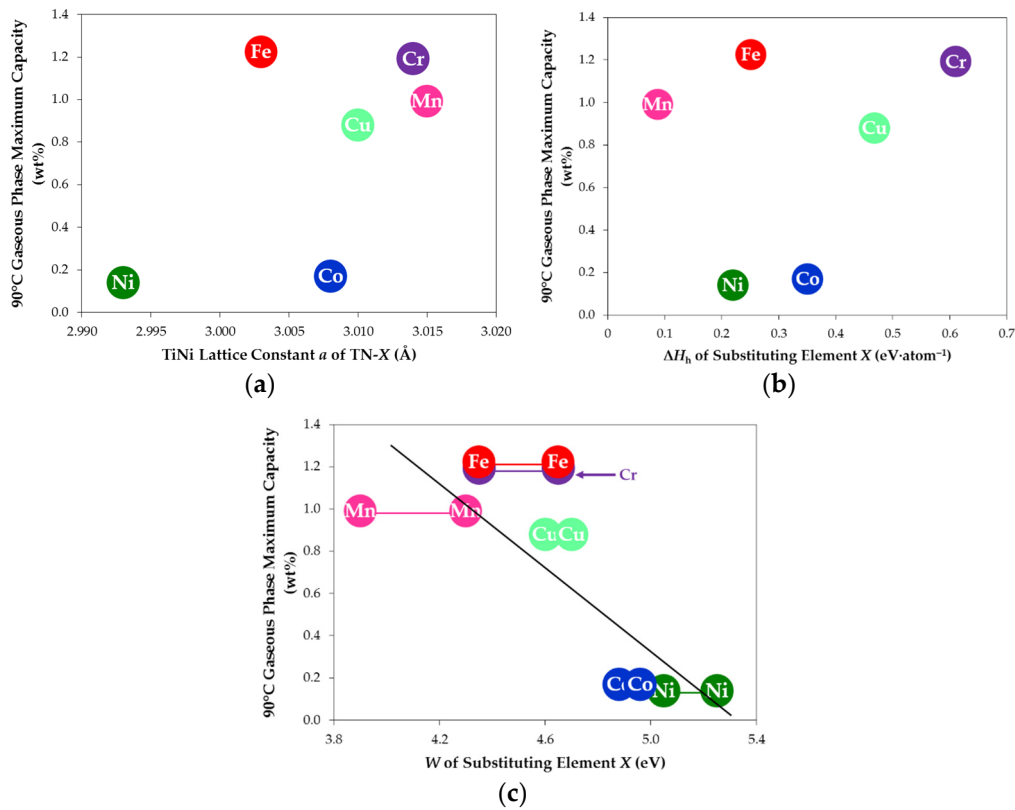
Figure 8. Plots of the 90 °C gaseous phase maximum capacity vs. (**a**) the corresponding TiNi lattice constant *a*; (**b**) ΔH_h of substituting element *X* (data from [16]); and (**c**) *W* of substituting element *X* (data from [81]). While the correlations with the TiNi lattice constant and ΔH_h of substituting element are weak, the increase in *W* of substituting element appears to have a negative effect on gaseous phase hydrogen storage.
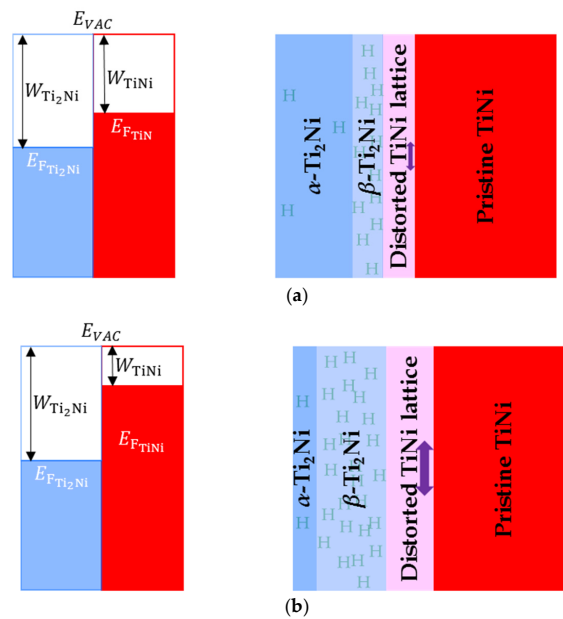

Figure 9. MH system composed of Ti_2Ni with higher *W* and TiNi with lower *W* before and after hydrogenation for (**a**) incorporation of substituting element with higher *W* (for example, Ni) in TiNi; and (**b**) incorporation for substituting element with lower *W* (for example, Cr) in TiNi.

3.5. Electrochemical Measurement

Discharge capacity performances of the six alloys were measured in a flooded cell configuration against a partially pre-charged $Ni(OH)_2$ positive electrode with 30 wt% KOH electrolyte. Electrodes were made with powder after PCT measurements. No alkaline pretreatment was applied before the half-cell measurement. For the discharge capacity measurement, the half-cell was first charged at a current density of 50 mA·g^{-1} for 10 h and then discharged at a current density of 50 mA·g^{-1} until a cut-off voltage of 0.9 V was reached. Then, the cell was discharged at a current density of 12 mA·g^{-1} until a cut-off voltage of 0.9 V was reached, and finally discharged at a current density of 4 mA·g^{-1} until a cut-off voltage of 0.9 V was reached. Full discharge capacities, specifically the sum of capacities measured at 50, 12, and 4 mA·g^{-1} for each cycle, from the first 10 cycles of the six alloys are plotted in Figure 10a to demonstrate activation and early cycling behaviors. Maximum full capacities, activation performances (the number of cycle needed to reach 95% of the maximum full capacity), and degradation performances (the ratio of the difference in maximum full capacity and full capacity at the tenth cycle to the maximum full capacity) are listed in Table 6. Capacity from the base alloy TN-Ni with a nominal composition of $Ti_{50}Zr_1Ni_{49}$ is higher than those from the stoichiometric TiNi alloys previously reported [13,14,27,29,38,39,46,47,50,53,57,58,64] due to the increase in DOD and formation of a considerable amount of the Ti_2Ni secondary phases. Most alloys are activated during the first cycle while alloys TN-Ni and TN-Cr take longer to fully activate, and alloys TN-Mn, TN-Co, and TN-Cu show more severe degradation. The lowest cycle stability is observed in alloy TN-Mn, and Mn's detrimental effects were also previously shown in the TiNi alloy [48,52]. Among all alloys, alloy TN-Fe does not only demonstrate the best balance between easy activation and cycle stability, it also has the highest full capacity of 397 mAh·g^{-1}, corresponding well with its highest gaseous phase capacity. Furthermore, capacities obtained from the gaseous phase and electrochemical measurements are compared in Figure 11, where the gaseous phase capacities are converted to their equivalent electrochemical capacities using the conversion factor 1 wt% H_2 = 268 mAh·g^{-1}. Gaseous phase capacities obtained at 30 °C are usually used for such comparison, but those cannot be measured due to the slow reaction kinetics of the alloys used in the current study. Therefore, 90 °C gaseous phase capacities are used. With the increasing atomic number of substituting elements, the electrochemical capacity first increases and then decreases. Increase in capacity due to the substitutions of Cr [49], Mn [48,52], Co [49,50], or Fe [38,50] and decrease in capacity from the substitution of Cu [52,66] in the TiNi-based alloys have been reported previously, and a comparative study of various substitutions has also shown a similar trend in electrochemical capacity compared to the results in this study. Moreover, electrochemical capacities of the six alloys are above the corresponding gaseous phase maximum capacities. Gaseous phase maximum capacity is composed of reversible and irreversible capacities and considered to be the upper bound for the electrochemical capacity, which usually falls between the boundaries set by the gaseous phase maximum and reversible capacities in most alloy systems [17,69,82–88]. Although increasing the temperature for the PCT measurements causes a reduction in gaseous phase maximum capacity [89] and consequently explains the out-of-bounds electrochemical capacities observed in most alloys, the tremendously large gaps between the electrochemical and gaseous phase maximum capacities for alloys TN-Ni and TN-Co indicate that the electrochemical environment is able to reduce the alloy system's equilibrium pressure and increases its capacity. Such a phenomenon has also been seen in the $ZrNi_5$-based alloys [90,91].

Half-cell HRDs, defined as the ratio of the discharge capacity measured at 50 mA·g^{-1} to that measured at 4 mA·g^{-1}, from the first 10 cycles of the six alloys are plotted in Figure 10b. All alloys achieve a stabilized HRD by the third cycle. HRDs at the second or third cycle (depends on where it is fully activated) of all alloys are listed in Table 6. HRDs of most alloys are better than that of alloy TN-Ni, with HRD of alloy TN-Cu being the highest. The Cu-substitution in the TiNi alloy formula [66] and later Cu-addition to the TiNi alloy [29] were shown to be beneficial to the high-rate performance. No obvious correlations can be found between HRD and structural properties (e.g., lattice constants,

phase abundances, and crystallite sizes). Although these HRDs are relatively low compared to those measured from the AB_2 [71,92], AB_5 [71], A_2B_7 [71], and Laves phase-related body-centered-cubic (bcc) solid solution MH alloys [17,87,88,93,94], some of the six alloys in the current study with higher capacities, e.g., alloy TN-Fe, can be used for high energy Ni/MH battery applications without strict power requirements.
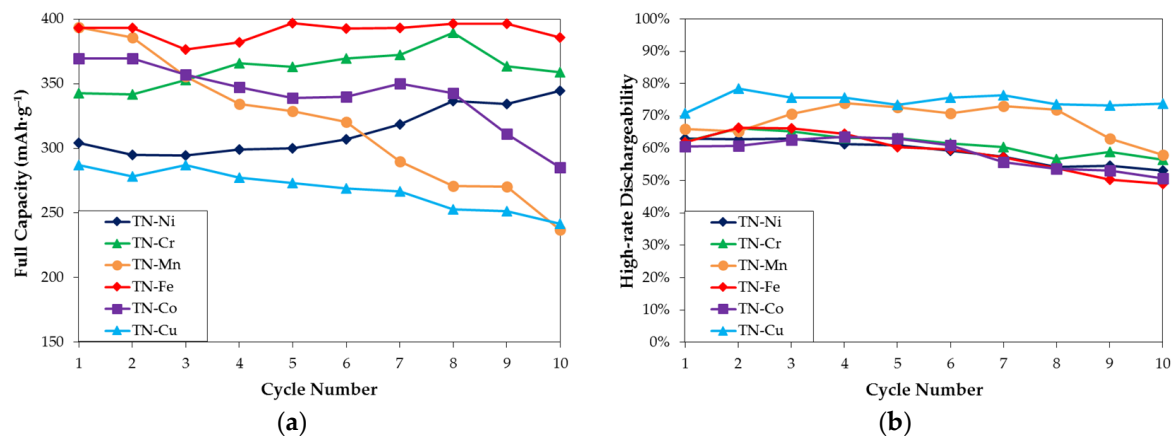

Figure 10. Activation and degradation behaviors observed from: (**a**) half-cell capacity measured at $4 \text{ mA} \cdot \text{g}^{-1}$; and (**b**) half-cell HRD for the first 10 cycles.

Table 6. Summary of room temperature electrochemical and magnetic susceptibility results.

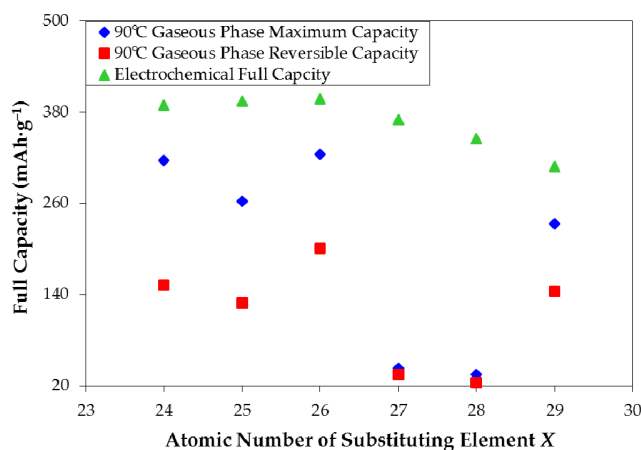| Alloy TN-*X*	TN-Ni	TN-Cr	TN-Mn	TN-Fe	TN-Co	TN-Cu
Maximum Full Capacity @4 mA·g^{-1} (mAh·g^{-1})	345	389	394	397	370	308
HRD @2nd or 3rd cycle (%)	63	66	71	66	63	79
Number of Cycles Needed to Reach 95% of Maximum Full Capacity	10	6	1	1	1	1
Degradation Performance (%)	0	8	40	3	23	21
D (10^{-10} cm^2·s^{-1})	3.15	2.71	2.68	1.87	2.37	1.94
I_o (mA·g^{-1})	22.15	24.77	34.08	37.47	26.19	36.43
M_s (emu·g^{-1})	0.187	0.219	0.509	0.511	0.586	0.542
$H_{1/2}$ (kOe)	0.172	0.221	0.170	0.159	0.151	0.484

Figure 11. Comparison of capacities obtained from the gaseous phase and electrochemical measurements. Gaseous phase capacity can be converted by 1 wt% = 268 mAh·g^{-1}.

Surface reaction exchange currents (I_o) and bulk hydrogen diffusion coefficients (D), two dominating factors in determining HRD, were measured electrochemically for the six alloys [69] and are listed in Table 6. All substitutions increase I_o but decrease D compared to the base alloy TN-Ni. Alloy TN-Fe, which exhibits the lowest D, also has the highest density of interface between the main TiNi and secondary Ti_2Ni phases. The channels for hydrogen transport between phases are abundant, however, they are also more tortuous in alloy TN-Fe and may negatively affect the bulk diffusion. By substituting the B-site with other transition metals that are more corrosion susceptible, not only does the activation become easier (Figure 10a), but more of the alloy surface is also dissolved away during activation, leaving more Ni embedded in the surface and consequently improving the surface reaction, although the Ni-content in the alloy formula is reduced. Both I_o and D are then correlated to HRD, and the resulting correlation factors are 0.24 and 0.46, respectively. Therefore, we conclude that the surface properties are more influential in determining HRD in the TiNi-based MH alloys. In addition, the D and I_o values of the six alloys in the current study are comparable to those obtained from the AB_2 [10,71,92], AB_5 [10,71], A_2B_7 [10,71], and Laves phase-related bcc solid solution MH alloys [17,87,88,94] and cannot explain their relatively low HRDs. Further investigation into other contributing factors affecting HRD of the TiNi-based MH alloys is needed.

3.6. Magnetic Properties

Magnetic susceptibility was used to characterize the nature of metallic nickel particles present in the surface layer of the alloy following an alkaline activation treatment [71]. Details of the background and experimental method have been reported earlier [95]. Metallic Ni is an active catalyst for the water splitting and recombination reactions that contributes to the I_o in the electrochemical system. This technique allows us to obtain the saturated magnetic susceptibility (M_s), a quantification of the amount of metallic Ni (the product of preferential oxidation) in the surface oxide, and the magnetic field strength at one-half of the M_s value ($H_{1/2}$), a measure of the averaged reciprocal number of Ni atoms in a metallic cluster. Magnetic susceptibility plots for the six alloys are shown in Figure 12, and the calculated M_s and $H_{1/2}$ values are listed in Table 6. Compared to alloy TN-Ni, M_ss of all substituted alloys are larger and correspond well with the overall observation in I_o. However, the largest M_s of 0.586 emu·g^{-1} is obtained from alloy TN-Co, which has a relatively low I_o among the substituted alloy. The $H_{1/2}$ values listed in Table 6 indicate that the sizes of metallic nickel are similar among most alloys except for alloy TN-Cu, which has much smaller metallic nickel particles in the surface and very high M_s. Both of these contribute to its high I_o, leading to alloy TN-Cu's impressive HRD performance among all alloys.
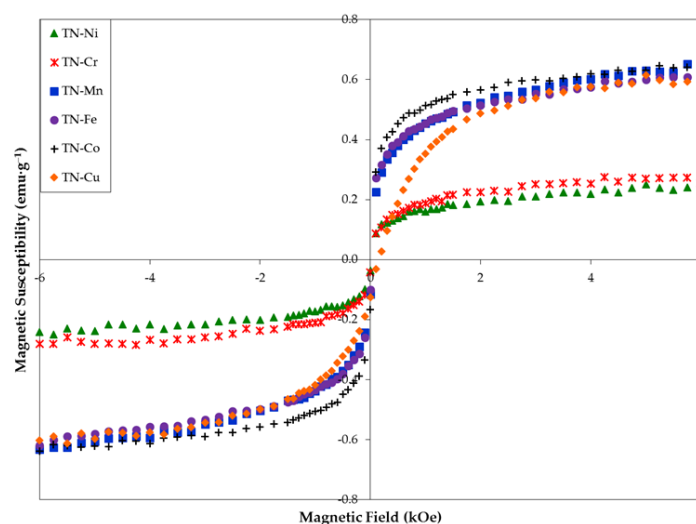

Figure 12. Magnetic susceptibility plots of the six alloys in the current study.

3.7. Comparison among Various Sbustitutions

Properties characterized from the gaseous phase and electrochemical measurements of the five substituted alloys compared to those of the base alloy TN-Ni are summarized in Table 7. Most of the properties are improved by substitution except for the bulk diffusion performance. Some general trends can also be observed: electrochemical capacity is inversely proportional to HRD, and HRD shows a similar trend compared to I_o and M_s. Among all substituted alloys, alloy TN-Fe has the best balance among capacity, HRD, activation and degradation performances and is recommended as the base alloy for further optimization.

Table 7. Performance comparison for the six alloys in the current study. +, −, or ≈ denote improved, deteriorated, or equal performance compared to the base alloy TN-Ni, respectively. Number of symbols indicates the degree of change compared to the base alloy TN-Ni.

Alloy TN-X	Gaseous Phase Capacity	Electrochemical Full Capacity	HRD	Activation	Degradation	D	I_o	M_s
TN-Cr	+ + + +	+ + + +	+	+ +	−	− −	+	+
TN-Mn	+ + +	+ + + + +	+ +	+ + + + +	− − − − −	− −	+ + + +	+ + + +
TN-Fe	+ + + + +	+ + + + +	+	+ + + + +	≈	− − − − −	+ + + + +	+ + + +
TN-Co	≈	+ +	≈	+ + + + +	− − −	− − −	+	+ + + + +
TN-Cu	+ + +	− − −	+ + + + +	+ + + + +	− −	− − − −	+ + + + +	+ + + + +

3.8. Property Comparison among Various Metal Hydride Alloy Systems

The general battery performances using various MH alloys are summarized in Table 8. In the table, AB$_5$, with a representative composition of $La_{10.5}Ce_{4.3}Pr_{0.5}Nd_{1.4}Ni_{60.0}Co_{12.7}Mn_{5.9}Al_{4.7}$, is the most widely used in the current consumer and transportation markets, and it has the best overall performance except for its relatively low capacity (320–330 mAh·g^{-1}). Significant research efforts on substitution have been performed with the AB$_5$ alloy to lower the cost and fulfill other specific requirements [10,96,97]. The AB$_2$ multi-phase alloy, with a very high capacity (420–436 mAh·g^{-1} [98]) and flexibility in composition [99,100], has great potential in ultra-low-temperature [101] and high-temperature applications due to the non-passive nature of its surface oxide [71]. The A$_2$B$_7$ superlattice-based multi-phase alloy family is the MH alloy currently used by FDK (Tokyo, Japan) for their Eneloop Ni/MH products. The A$_2$B$_7$ alloy, with a representative composition of $La_{3.3}Ce_8Pr_8Mg_{3.9}Ni_{72.8}Al_{4.0}$, has a marginally improved capacity (355 mAh·g^{-1}) over the conventional AB$_5$ but also a tradeoff with regard to cycle stability due to the incorporation of Mg, which can be solved by adding the proper binder to the negative electrode [102]. Works related to the improvement in capacity and low-temperature performance have been previously reported by authors [103–107]. The bcc alloy has a very high theoretical capacity (1072 mAh·g^{-1}) but a much lower reported capacity (247 mAh·g^{-1}) for the composition $Ti_{40}V_{30}Cr_{15}Mn_{13}Mo_2$, and its stability is very poor, requiring an electrolyte with much lower corrosion capability, for example, ionic liquid [108]. The high cost of V is also a concern for utilizing the bcc alloy in any practical applications. The Laves phase-related bcc alloy was developed through a U.S. Department of Energy sponsored program, and the resulted alloy has a composition of $Ti_{14.5}Zr_{2.7}V_{46.6}Cr_{11.9}Mn_{6.5}Co_{1.5}Ni_{16.9}Al_{0.4}$ and a capacity of 414 mAh·g^{-1} [17,94,109], which was recommended for electric vehicle applications running at a C/3 discharge rate. The MgNi-based amorphous alloy made by mechanical alloying has a very attractive cost model and an ultra-high capacity (780 mAh·g^{-1} for the composition $Mg_{52}Ni_{39}Co_3Mn_6$), but it suffers in cycle stability in 30 wt% KOH electrolyte [18]. Studies that address changes in anions of the hydroxides used [18] and additions of various salts [110] have been developed to extend the usable cycles of the MgNi-based alloy. The last row in Table 8 is the main subject of this paper—the TiNi alloy family. TiNi at the current stage is not suitable for either consumer electronic or propulsion applications that require a decent HRD. However, its low cost and long cycle life make the TiNi alloy perfect for stationary applications. Therefore, testing of the TiNi-based alloys at different temperatures will be our next task.

Table 8. Performance comparison among various MH alloy families. The number of stars indicates the superiority in the performance category. TBD and Temp. denote to-be-determined and temperature, respectively.

Alloy	Cost	Capacity	HRD	Activation	Low Temp.	High Temp.	Charge Retention	Cycle Life
AB_5	★★★★	★	★★★★★	★★★★★	★★★★	★★	★★★★	★★★★★
AB_2	★★★	★★★★	★★★★	★★★	★★★★★	★★★★★	★★★	★★★★★
A_2B_7	★★★	★★	★★★★★	★★★★★	★★★★★	★★★	★★★★★	★★★★
bcc	★★	★★★★★	★★	★★★★★	TBD	TBD	★	★
Laves-bcc	★	★★★★	★★★	★★★★	★★★	★★	★	★★★
MgNi	★★★★★	★★★★★	★★	★★★★★	TBD	TBD	TBD	★
TiNi	★★★★★	★★★	★	★★	TBD	TBD	TBD	★★★★★

4. Conclusions

Structural, magnetic, gaseous phase hydrogen storage, and electrochemical properties of a series of $Ti_{50}Zr_1Ni_{44}X_5$ (X = Ni, Cr, Mn, Fe, Co, or Cu) metal hydride alloys were investigated. All alloys show similar multi-phase distributions composed of a stoichiometric TiNi matrix, a hyperstoichiometric TiNi minor phase, and a Ti_2Ni secondary phase. Compared to the $Ti_{50}Zr_1Ni_{49}$ base alloy, substituting element with higher work function enhances the synergetic effects between the main TiNi and secondary Ti_2Ni phases and increases the gaseous phase hydrogen storage capacity substantially. Moreover, the electrochemical environment is able to reduce the alloy system's equilibrium pressure and further improves the capacity. The TiNi-based alloys have a superb cost model and exhibit satisfactory capacity and cycle life performances, however, these alloys score low in high-rate performance despite their similar surface reaction, bulk diffusion, and magnetic properties to the commonly used AB_5, AB_2, and A_2B_7 alloys. Among the alloys investigated, alloy with the composition $Ti_{50}Zr_1Ni_{44}Fe_5$ demonstrates the best balance among capacity, high-rate performance, activation, and cycle stability and is recommended for full-cell testing at various temperatures to validate its practicality for high-energy or stationary applications. $Ti_{50}Zr_1Ni_{44}Fe_5$ will also be used as the base composition for formula optimization in the future.

Author Contributions: Jean Nei conceived and performed the experiments, and Kwo-Hsiung Young participated in data interpretation and paper preparation.

Conflicts of Interest: The authors declare no conflicts of interest.

Abbreviations

Ni/MH	Nickel/metal hydride
MH	Metal hydride
HRD	High-rate dischargeability
ΔH_h	Heat of hydride formation
SN	Sintering
AM	Arc melting
PM	Melting in a plasma furnace
IM	Induction melting
CO	Co-precipitation
MC	Microencapsulation
MA	Mechanical alloying
ANN	Annealing
MS	Melt spinning
CHR	Calcium hydride reduction
MWCNT	Multiwall carbon nanotube
ICP	Inductively coupled plasma spectrometer/spectrometry
XRD	X-ray diffractometer/diffraction

SEM	Scanning electron microscope/microscopy
EDS	Energy dispersive spectroscopy
PCT	Pressure-concentration-temperature
W	Work function
E_{VAC}	Electron potential in vacuum (E_{VAC}) and the Fermi level (E_F)
E_F	Electron potential in the Fermi level
bcc	Body-centered-cubic
I_o	Surface reaction exchange current
D	Bulk hydrogen diffusion coefficient
M_s	Saturated magnetic susceptibility
$H_{1/2}$	Magnetic field strength at one-half of the saturated magnetic susceptibility value

References

1. Zelinsky, M.; Koch, J.; Fetcenko, M. Heat Tolerant NiMH Batteries for Stationary Power. Available online: http://www.battcon.com/PapersFinal2010/ZelinskyPaper2010Final_12.pdf (accessed on 5 May 2016).

2. Zelinsky, M.; Koch, J. Batteries and Heat—A Recipe for Success? Available online: http://www.battcon.com/PapersFinal2013/16-Mike%20Zelinsky%20-%20Batteries%20and%20Heat.pdf (accessed on 5 May 2016).

3. Wikipedia, the Free Encyclopedia. General Motors EV1. Available online: https://en.wikipedia.org/wiki/General_Motors_EV1 (accessed on 20 June 2016).

4. The Jaffes. EV1. Available online: http://thejaffes.org/content/ev1 (accessed on 20 June 2016).

5. Sakintuna, B.; Lamari-Darkrim, F.; Hirscher, M. Metal hydride materials for solid hydrogen storage: A review. *Int. J. Hydrog. Energy* **2007**, *32*, 1121–1140. [CrossRef]

6. Paul-Boncour, V. Metal hydrides for hydrogen storage. *J. Adv. Sci.* **2007**, *19*, 16–21. [CrossRef]

7. Zhao, X.; Ma, L. Recent progress in hydrogen storage alloys for nickel/metal hydride secondary batteries. *Int. J. Hydrog. Energy* **2009**, *34*, 4788–4796. [CrossRef]

8. Pukszhselvan, D.; Kumar, V.; Singh, S.K. High capacity hydrogen storage: Basic aspects, new developments and milestones. *Nano Energy* **2012**, *1*, 566–589. [CrossRef]

9. Klebanoff, L.E.; Keller, J.O. 5 Years of hydrogen storage research in the U.S. DOE Metal Hydride Center of Excellence (MHCoE). *Int. J. Hydrog. Energy* **2013**, *38*, 4533–4576. [CrossRef]

10. Young, K.; Nei, J. The current status of hydrogen storage alloy development for electrochemical applications. *Materials* **2013**, *6*, 4574–4608. [CrossRef]

11. Young, K. Metal Hydrides. In *Reference Module in Chemistry, Molecular Sciences and Chemical Engineering*; Elsevier B.V.: Waltham, MA, USA, 2013.

12. Liu, W.; Webb, C.J.; Gray, E.M. Review of hydrogen storage in AB$_3$ alloys targeting stationary fuel cell applications. *Int. J. Hydrog. Energy* **2016**, *41*, 3485–3507. [CrossRef]

13. Gutjahr, M.A.; Buchner, H.; Beccu, K.D.; Säufferer, H. A New Type of Reversible Negative Electrode for Alkaline Storage Batteries Based on Metal Alloy Hydrides. In *Power Sources*; Collins, D.H., Wada, K., Hiraki, A., Eds.; Oriel Press: Newcastle upon Tyne, UK, 1973; Volume 4, pp. 79–91.

14. Beccu, K. Negative Electrode of Titanium-Nickel Alloy Hydride Phases. U.S. Patent 3,824,131, 16 July 1974.

15. Murray, J.L. Ni-Ti (Nickel-Titanium). In *Binary Alloy Phase Diagram*, 2nd ed.; Massalski, T.B., Okamoto, H., Subramanian, P.R., Kacprzak, L., Eds.; ASM International: Materials Park, OH, USA, 1990; Volume 3, pp. 2874–2876.

16. Osumi, Y. *Hydrogen Absorbing Alloy—The Physical Properties and Applications*, 1st ed.; Agune Technology Center: Tokyo, Japan, 1993; p. 73.

17. Young, K.; Ouchi, T.; Meng, T.; Wong, D.F. Studies on the synergetic effects in multi-phase metal hydride alloys. *Batteries* **2016**, *2*. [CrossRef]

18. Nei, J.; Young, K.; Rotarov, D. Studies on MgNi-based metal hydride electrode with aqueous electrolytes composed of various hydroxides. *Batteries* **2016**, *2*. [CrossRef]

19. Justi, E.W.; Ewe, H.H.; Kalberlah, A.W.; Saridakis, N.M.; Schaefer, M.H. Electrocatalysis in the nickel-titanium system. *Energy Convers.* **1970**, *10*, 183–187. [CrossRef]

20. Miles, M.H. Evaluation of electrocatalysts for water electrolysis in alkaline solutions. *J. Electroanal. Chem. Interfacial Electrochem.* **1975**, *60*, 89–96. [CrossRef]

21. Wakao, S.; Yonemura, Y.; Nakano, H.; Shimada, H. Electrochemical capacities and corrosion of TiNi$_x$ and its zirconium-substituted alloy hydride electrodes. *J. Less Common Met.* **1984**, *104*, 365–373. [CrossRef]

22. Wakao, S.; Nakano, H.; Chubachi, S. Behaviour of hydrogen-absorbing metal alloys in an alkaline solution containing hydrazine. *J. Less Common Met.* **1984**, *104*, 385–393. [CrossRef]

23. Wakao, S.; Sawa, H.; Nakano, H.; Chubachi, S.; Abe, M. Capacities and durabilities of Ti-Zr-Ni alloy hydride electrodes and effects of electroless plating on their performances. *J. Less Common Met.* **1987**, *131*, 311–319. [CrossRef]

24. Song, D.; Gao, X.; Zhang, Y.; Lin, D.; Zhou, Z.; Wang, G.; Shen, P. Surface analysis of a Ti-Ni-B hydrogen storage electrode. *J. Alloys Compd.* **1993**, *199*, 161–163.

25. Jordy, C.; Latroche, M.; Percheron-Guégan, A.; Achard, J.C. Effect of partial substitution in TiNi on its structural and electrochemical hydrogen storage properties. *Z. Phys. Chem.* **1994**, *185*, 119–130. [CrossRef]

26. Yan, D.-Y. Catalytic effects of alloy surface on the oxygen consumption reaction in a sealed Ni/TiNiH battery. *J. Alloys Compd.* **1994**, *209*, 257–261. [CrossRef]

27. Wang, C.; Lei, Y.; Yang, X.; Jiang, J.; Wu, J.; Wang, Q. Effects of phase structures of TiNi on the electrochemical properties. *Acta Metall. Sin.* **1995**, *31*, 440–444.

28. Lei, Y.Q.; Wang, C.S.; Yang, X.G.; Pan, H.G.; Wu, J.; Wang, Q.D. A mathematical model for the cycle life of hydride electrodes. *J. Alloys Compd.* **1995**, *231*, 611–615. [CrossRef]

29. Liu, J.; Gao, X.; Song, D.; Zhang, Y.; Ye, S. The characteristics of the microencapsulated Ti-Ni alloys and their electrodes. *J. Alloys Compd.* **1995**, *231*, 852–855.

30. Jung, C.B.; Lee, K.S. Electrode characteristics of metal hydride electrodes prepared by mechanical alloying. *J. Alloys Compd.* **1997**, *253–254*, 605–608. [CrossRef]

31. Jung, C.B.; Kim, J.H.; Lee, K.S. Electrode characteristics of nanostructured TiFe and $ZrCr_2$ type metal hydride prepared by mechanical alloying. *Nanostructured Mater.* **1997**, *8*, 1093–1104. [CrossRef]

32. Wang, C.S.; Lei, Y.Q.; Wang, Q.D. Effects of Nb and Pd on the electrochemical properties of a Ti-Ni hydrogen-storage electrode. *J. Power Sources* **1998**, *70*, 222–227. [CrossRef]

33. Wang, C.S.; Lei, Y.Q.; Wang, Q.D. Studies of electrochemical properties of TiNi alloy used as an MH electrode—I. Discharge capacity. *Electrochim. Acta* **1998**, *43*, 3193–3207. [CrossRef]

34. Wang, C.S.; Lei, Y.Q.; Wang, Q.D. Studies of electrochemical properties of TiNi alloy used as an MH electrode. II. Discharge kinetics. *Electrochim. Acta* **1998**, *43*, 3209–3216. [CrossRef]

35. Zhang, Q.A.; Lei, Y.Q.; Wang, C.S.; Wang, F.S.; Wang, Q.D. Structure of the secondary phase and its effects on hydrogen-storage properties in a $Ti_{0.7}Zr_{0.2}V_{0.1}Ni$ alloy. *J. Power Sources* **1998**, *75*, 288–291. [CrossRef]

36. Han, S.S.; Goo, N.H.; Jeong, W.T.; Lee, K.S. Synthesis of composite metal hydride alloy of A_2B and AB type by mechanical alloying. *J. Power Sources* **2001**, *92*, 157–162. [CrossRef]

37. Cuevas, F.; Latroche, M.; Ochin, P.; Dezellus, A.; Fernández, J.F.; Sánchez, C.; Percheron-Guégan, A. Influence of the martensitic transformation on the hydrogenation properties of $Ti_{50-x}Zr_xNi_{50}$ alloys. *J. Alloys Compd.* **2002**, *330–332*, 250–255. [CrossRef]

38. Jurczyk, M.; Jankowska, E.; Nowak, M.; Jakubowicz, J. Nanocrystalline titanium-type metal hydride electrodes prepared by mechanical alloying. *J. Alloys Compd.* **2002**, *336*, 265–269. [CrossRef]

39. Bobet, J.; Chevalier, B. Reactive mechanical grinding applied to a (Ti + Ni) mixture and to a TiNi compound. *Intermetallics* **2002**, *10*, 597–601. [CrossRef]

40. Xu, Y.H.; Chen, C.P.; Wang, X.L.; Wang, Q.D. The analysis of the two discharge plateaus for Ti-Ni-based metal hydride electrode alloys. *J. Power Sources* **2002**, *112*, 105–108. [CrossRef]

41. Szajek, A.; Jurczyk, M.; Jankowska, E. The electronic and electrochemical properties of the TiFe-based alloys. *J. Alloys Compd.* **2003**, *348*, 285–292. [CrossRef]

42. Jurczyk, M.; Jankowska, E.; Makowiecka, M.; Wieczorek, I. Electrode characteristics of nanocrystalline TiFe-type alloys. *J. Alloys Compd.* **2003**, *354*, L1–L4. [CrossRef]

43. Han, S.S.; Goo, N.H.; Lee, K.S. Effects of sintering on composite metal hydride alloy of Mg_2Ni and TiNi synthesized by mechanical alloying. *J. Alloys Compd.* **2003**, *360*, 243–249. [CrossRef]

44. Zhang, Q.A.; Lei, Y.Q. Multi-component TiNi-based hydrogen storage alloys with the secondary Laves phase. *J. Alloys Compd.* **2004**, *368*, 362–366. [CrossRef]

45. Jankowska, E.; Jurczyk, M. Electrochemical properties of sealed Ni-MH batteries using nanocrystalline TiFe-type anodes. *J. Alloys Compd.* **2004**, *372*, L9–L12. [CrossRef]

46. Makowiecka, M.; Jankowska, E.; Okonska, I.; Jurczyk, M. Effect of Zr additions on the electrode characteristics of nanocrystalline TiNi-type hydrogen storage alloys. *J. Alloys Compd.* **2005**, *388*, 303–307. [CrossRef]

47. Shcherbakova, L.G.; Solonin, S.M.; Kolomiets, L.L.; Katashinskii, V.P. Effect of phase composition and activation of a titanium nickelide surface by electrochemical cycling on its hydrogen sorption capacity. *Powder Metall. Met. Ceram.* **2005**, *44*, 389–395. [CrossRef]

48. Szajek, A.; Makowiecka, M.; Jankowska, E.; Jurczyk, M. Electrochemical and electronic properties of nanocrystalline TiNi$_{1-x}$M$_x$ (M = Mg, Mn, Zr, x = 0, 0.125, 0.25) ternary alloys. *J. Alloys Compd.* **2005**, *403*, 323–328. [CrossRef]

49. Jankowska, E.; Makowiecka, M.; Jurczyk, M. Nickel-metal hydride battery using nanocrystalline TiFe-type hydrogen storage alloys. *J. Alloys Compd.* **2005**, *404–406*, 691–693. [CrossRef]

50. Drenchev, B.; Spassov, T. Electrochemical hydriding of amorphous and nanocrystalline TiNi-based alloys. *J. Alloys Compd.* **2007**, *441*, 197–201. [CrossRef]

51. Jankowska, E.; Makowiecka, M.; Jurczyk, M. Electrochemical performance of sealed Ni-MH batteries using nanocrystalline TiNi-type hydride electrodes. *Renew. Energy* **2008**, *33*, 211–215. [CrossRef]

52. Drenchev, B.; Spassov, T.; Radev, D. Influence of alloying and microstructure on the electrochemical hydriding of TiNi-based ternary alloys. *J. Appl. Electrochem.* **2008**, *38*, 437–444. [CrossRef]

53. Guiose, B.; Cuevas, F.; Décamps, B.; Percheron-Guégan, A. Solid-gas and electrochemical hydrogenation properties of pseudo-binary (Ti,Zr)Ni intermetallic compounds. *Int. J. Hydrog. Energy* **2008**, *33*, 5795–5800. [CrossRef]

54. Drenchev, B.; Spassov, T. Influence of B substitution for Ti and Ni on the electrochemical hydriding of TiNi. *J. Alloys Compd.* **2009**, *474*, 527–530. [CrossRef]

55. Guiose, B.; Cuevas, F.; Décamps, B.; Leroy, E.; Percheron-Guégan, A. Microstructural analysis of the ageing of pseudo-binary (Ti,Zr)Ni intermetallic compounds as negative electrodes of Ni-MH batteries. *Electrochim. Acta* **2009**, *54*, 2781–2789. [CrossRef]

56. Qu, X.; Ma, L.; Yang, M.; Ding, Y. Effect of sintering temperature on electrochemical properties of TiNi hydrogen storage alloy. *Chin. J. Rare Met.* **2010**, *34*, 331–335.

57. Yang, M.; Zhao, X.; Ding, Y.; Ma, L.; Qu, X.; Gao, Y. Electrochemical properties of titanium-based hydrogen storage alloy prepared by solid phase sintering. *Int. J. Hydrog. Energy* **2010**, *35*, 2717–2721. [CrossRef]

58. Zhao, X.; Ma, L.; Yang, M.; Ding, Y.; Shen, X. Electrochemical properties of Ti-Ni-H powders prepared by milling titanium hydride and nickel. *Int. J. Hydrog. Energy* **2010**, *35*, 3076–3079. [CrossRef]

59. Jiang, X.; Liu, Q.; Zhang, L. Electrochemical hydrogen storage property of NiTi alloys with different Ti content prepared by mechanical alloying. *Rare Met.* **2011**, *30*, 63–67. [CrossRef]

60. Zlatanova, Z.; Spassov, T.; Eggeler, G.; Spassova, M. Synthesis and hydriding/dehydriding properties of Mg$_2$Ni-AB (AB = TiNi or TiFe) nanocomposites. *Int. J. Hydrog. Energy* **2011**, *36*, 7559–7566. [CrossRef]

61. Emami, H.; Cuevas, F. Hydrogenation properties of shape memory Ti(Ni,Pd) compounds. *Intermetallics* **2011**, *19*, 876–886. [CrossRef]

62. Hu, R.; Liu, H.; Zeng, M.; Liu, J.; Zhu, M. Influence of Sn content on microstructure and electrochemical properties of Sn-NiTi film anodes in lithium ion batteries. *J. Power Sources* **2012**, *244*, 456–462. [CrossRef]

63. Bououdina, M.; Oumellal, Y.; Dupont, L.; Aymard, L.; Al-Gharni, H.; Al-Hajry, A.; Maark, T.A.; De Sarkar, A.; Ahuja, R.; Deshpande, M.D.; et al. Lithium storage in amorphous TiNi hydride: Electrode for rechargeable lithium-ion batteries. *Mater. Chem. Phys.* **2013**, *141*, 348–354. [CrossRef]

64. Balcerzak, M.; Nowak, M.; Jakubowicz, J.; Jurczyk, M. Electrochemical behavior of nanocrystalline TiNi doped by MWCNTs and Pd. *Renew. Energy* **2014**, *62*, 432–438. [CrossRef]

65. Li, X.D.; Elkedim, O.; Nowak, M.; Jurczyk, M. Characterization and first principle study of ball milled Ti-Ni with Mg doping as hydrogen storage alloy. *Int. J. Hydrog. Energy* **2014**, *39*, 9735–9743. [CrossRef]

66. Emami, H.; Cuevas, F.; Latroche, M. Ti(Ni,Cu) pseudobinary compounds as efficient negative electrodes for Ni-MH batteries. *J. Power Sources* **2014**, *265*, 182–191. [CrossRef]

67. Zhang, Z.; Elkedim, O.; Balcerzak, M.; Jurczyk, M. Structural and electrochemical hydrogen storage properties of MgTiN$_x$ (x = 0.1, 0.5, 1, 2) alloys prepared by ball milling. *Int. J. Hydrog. Energy* **2016**. in press.

68. Balcerzak, M. Electrochemical and structural studies on Ti-Zr-Ni and Ti-Zr-Ni-Pd alloys and composites. *J. Alloys Compd.* **2016**, *658*, 576–587. [CrossRef]

69. Nei, J.; Young, K.; Salley, S.O.; Ng, K.Y.S. Effects of annealing on Zr$_8$Ni$_{19}$X$_2$ (X = Ni, Mg, Al, Sc, V, Mn, Co, Sn, La, and Hf): Hydrogen storage and electrochemical properties. *Int. J. Hydrog. Energy* **2012**, *37*, 8418–8427. [CrossRef]

70. Hasson, D.F.; Arsenault, R.J. Substitutional-Interstitial Interactions in bcc Alloys. In *Treatise on Materials Science and Technology: Materials Science Series*; Herman, H., Ed.; Academic Press: New York, NY, USA, 1972; Volume 1, p. 218.

71. Young, K.; Huang, B.; Regmi, R.K.; Lawes, G.; Liu, Y. Comparisons of metallic clusters imbedded in the surface of AB_2, AB_5, and A_2B_7 alloys. *J. Alloys Compd.* **2010**, *506*, 831–840. [CrossRef]

72. Kokalj, A. Computer graphics and graphical user interfaces as tools in simulations of matter at the atomic scale. *Comput. Mater. Sci.* **2003**, *28*, 155–168. [CrossRef]

73. Dwight, A.E. CsCl-type equiatomic phases in binary alloys of transition elements. *Trans. Am. Inst. Min. Metall. Pet. Eng.* **1959**, *215*, 283–286.

74. The Japan Institute of Metals and Materials. *Non-Stoichiometric Metal Compounds*; Maruzen: Tokyo, Japan, 1975; p. 296.

75. Klug, H.P.; Alexander, L.E. *X-Ray Diffraction Procedures: For Polycrystalline and Amorphous Materials*, 2nd ed.; John Wiley & Sons: New York, NY, USA, 1974; p. 656.

76. Bohnenstiehl, S.D.; Susner, M.A.; Dregia, S.A.; Sumption, M.D.; Donovan, J.; Collings, E.W. Experimental determination of the peritectic transition temperature of MgB_2 in the Mg-B phase diagram. *Thermochim. Acta* **2014**, *576*, 27–35. [CrossRef]

77. Yen, F.; Hwang, K. Shape memory characteristics and mechanical properties of high-density powder metal TiNi with post-sintering heat treatment. *Mater. Sci. Eng. A* **2011**, *528*, 5296–5305. [CrossRef]

78. Gupta, K.P. The Ni-Ti-Zr system (nickel-titanium-zirconium). *J. Phase Equilib.* **1999**, *20*, 441–448. [CrossRef]

79. Osumi, Y. *Hydrogen Absorbing Alloy—The Physical Properties and Applications*, 1st ed.; Agune Technology Center: Tokyo, Japan, 1993; p. 57.

80. Liu, Y.; Young, K. Microstructure investigation on metal hydride alloys by electron backscatter diffraction technique. *Batteries* **2016**, *2*. [CrossRef]

81. Drummond, T.J. *Work Functions of the Transition Metals and Metal Silicides*; SAND99-0391J; Sandia National Labs.: Albuquerque, NM, USA; Livermore, CA, USA, 1999.

82. Sun, D.; Jiang, J.; Lei, Y.; Liu, W.; Wu, J.; Wang, Q.; Yang, G. Effects of measurement factor on electrochemical capacity of some hydrogen storage alloys. *Mater. Sci. Eng. B* **1995**, *30*, 19–22. [CrossRef]

83. Young, K.; Fetcenko, M.A.; Li, F.; Ouchi, T. Structural, thermodynamic, and electrochemical properties of $Ti_xZr_{1-x}(VNiCrMnCoAl)_2$ C14 Laves phase alloys. *J. Alloys Compd.* **2008**, *464*, 238–247. [CrossRef]

84. Young, K.; Nei, J.; Huang, B.; Ouchi, T.; Fetcenko, M.A. Studies of $Ti_{1.5}Zr_{5.5}V_{0.5}(M_xNi_{1-x})9.5$ (M = Cr, Mn, Fe, Co, Cu, Al): Part 2. Hydrogen storage and electrochemical properties. *J. Alloys Compd.* **2010**, *501*, 245–254. [CrossRef]

85. Young, K.; Chao, B.; Huang, B.; Nei, J. Studies on the hydrogen storage characteristic of $La_{1-x}Ce_x(NiCoMnAlCuSiZr)_{5.7}$ with a B2 secondary phase. *J. Alloys Compd.* **2014**, *585*, 760–770. [CrossRef]

86. Young, K.; Wong, D.F.; Wang, L. Effect of Ti/Cr content on the microstructures and hydrogen storage properties of Laves phase-related body-centered-cubic solid solution alloys. *J. Alloys Compd.* **2015**, *622*, 885–893. [CrossRef]

87. Young, K.; Ouchi, T.; Nei, J.; Meng, T. Effects of Cr, Zr, V, Mn, Fe, and Co to the hydride properties of Laves phase-related body-centered-cubic solid solution alloys. *J. Power Sources* **2015**, *281*, 164–172. [CrossRef]

88. Young, K.; Ouchi, T.; Nei, J.; Wang, L. Annealing effects on Laves phase-related body-centered-cubic solid solution metal hydride alloys. *J. Alloys Compd.* **2016**, *654*, 216–225. [CrossRef]

89. Young, K. Stoichiometry in Inter-Metallic Compounds for Hydrogen Storage Applications. In *Stoichiometry and Materials Science—When Numbers Matter*; Innocenti, A., Kamarulzaman, N., Eds.; Intech: Rijeka, Crotia, 2012; p. 150.

90. Young, K.; Young, M.; Chang, S.; Huang, B. Synergetic effects in electrochemical properties of $ZrV_xNi_{4.5-x}$ (x = 0.0, 0.1, 0.2, 0.3, 0.4, and 0.5) metal hydride alloys. *J. Alloys Compd.* **2013**, *560*, 33–41. [CrossRef]

91. Mosavati, N.; Young, K.; Meng, T.; Ng, K.Y.S. Electrochemical open-circuit voltage and pressure-concentration-temperature isotherm comparison for metal hydride alloys. *Batteries* **2016**, *2*. [CrossRef]

92. Young, K.; Ouchi, T.; Lin, X.; Reichman, B. Effects of Zn-addition to C14 metal hydride alloys and comparisons to Si, Fe, Cu, Y, and Mo-additives. *J. Alloys Compd.* **2016**, *655*, 50–59. [CrossRef]

93. Young, K.; Nei, J.; Wong, D.F.; Wang, L. Structural, hydrogen storage, and electrochemical properties of Laves phase-related body-centered-cubic solid solution metal hydride alloys. *Int. J. Hydrog. Energy* **2014**, *39*, 21489–21499. [CrossRef]

94. Young, K.; Wong, D.F.; Nei, J. Effects of vanadium/nickel contents in Laves phase-related body-centered-cubic solid solution metal hydride alloys. *Batteries* **2015**, *1*, 34–53. [CrossRef]

95. Nei, J.; Young, K.; Regmi, R.; Lawes, G.; Salley, S.O.; Ng, K.Y.S. Gaseous phase hydrogen storage and electrochemical properties of Zr_8Ni_{21}, Zr_7Ni_{10}, Zr_9Ni_{11}, and ZrNi metal hydride alloys. *Int. J. Hydrog. Energy* **2012**, *37*, 16042–16055. [CrossRef]

96. Young, K.; Ouchi, T.; Reichman, B.; Koch, J.; Fetcenko, M.A. Improvement in the low-temperature performance of AB_5 metal hydride alloys by Fe-addition. *J. Alloys Compd.* **2011**, *509*, 7611–7617. [CrossRef]

97. Young, K.; Yasuoka, S. Capacity degradation mechanisms in nickel/metal hydride batteries. *Batteries* **2016**, *2*. [CrossRef]

98. Young, K.; Ouchi, T.; Koch, J.; Fetcenko, M.A. The role of Mn in C14 Laves phase multi-component alloys for NiMH battery application. *J. Alloys Compd.* **2009**, *477*, 749–758. [CrossRef]

99. Chang, S.; Young, K.; Ouchi, T.; Meng, T.; Nei, J.; Wu, X. Studies on incorporation of Mg in Zr-based AB_2 metal hydride alloys. *Batteries* **2016**, *2*. [CrossRef]

100. Young, K.; Ouchi, T.; Nei, J.; Moghe, D. Importance of rare-earth additions in Zr-based AB_2 metal hydride alloys. *Batteries* **2016**, *2*. [CrossRef]

101. Young, K.; Wong, D.F.; Ouchi, T.; Huang, B.; Reichman, B. Effects of La-addition to the structure, hydrogen storage, and electrochemical properties of C14 metal hydride alloys. *Electrochim. Acta* **2015**, *174*, 815–825. [CrossRef]

102. Ouchi, T.; Young, K.; Moghe, D. Reviews on the Japanese patent applications regarding nickel/metal hydride batteries. *Batteries* **2016**, *2*. [CrossRef]

103. Young, K.; Wong, D.F.; Wang, L.; Nei, J.; Ouchi, T.; Yasuoka, S. Mn in misch-metal based superlattice metal hydride alloy—Part 1 structural, hydrogen storage and electrochemical properties. *J. Power Sources* **2015**, *277*, 426–432. [CrossRef]

104. Young, K.; Koch, J.; Yasuoka, S.; Shen, H.; Bendersky, L.A. Mn in misch-metal based superlattice metal hydride alloy—Part 2 Ni/MH battery performance and failure mechanism. *J. Power Sources* **2015**, *277*, 433–442. [CrossRef]

105. Wang, L.; Young, K.; Meng, T.; Ouchi, T.; Yasuoka, S. Partial substitution of cobalt for nickel in mixed rare earth metal based superlattice hydrogen absorbing alloy—Part 1 Structural, hydrogen storage and electrochemical properties. *J. Alloys Compd.* **2016**, *660*, 407–415. [CrossRef]

106. Wang, L.; Young, K.; Meng, T.; English, N.; Yasuoka, S. Partial substitution of cobalt for nickel in mixed rare earth metal based superlattice hydrogen absorbing alloy—Part 2 Battery performance and failure mechanism. *J. Alloys Compd.* **2016**, *664*, 417–427. [CrossRef]

107. Meng, T.; Young, K.; Koch, J.; Ouchi, T.; Yasuoka, S. Failure mechanisms of nickel/metal hydride batteries with cobalt-substituted superlattice hydrogen-absorbing alloy anodes at 50 °C. *Batteries* **2016**, *2*. [CrossRef]

108. Young, K.; Ouchi, T.; Huang, B.; Nei, J. Structure, hydrogen storage, and electrochemical properties of body-centered-cubic $Ti_{40}V_{30}Cr_{15}Mn_{13}X_2$ alloys (*X* = B, Si, Mn, Ni, Zr, Nb, Mo, and La). *Batteries* **2015**, *1*, 74–90. [CrossRef]

109. Young, K.; Ng, K.Y.S.; Bendersky, L.A. A technical report of the robust affordable next generation energy storage system-BASF program. *Batteries* **2016**, *2*. [CrossRef]

110. Yan, S.; Young, K.; Ng, K.Y.S. Effects of salt additives to the KOH electrolyte used in Ni/MH batteries. *Batteries* **2015**, *1*, 54–73. [CrossRef]